Journal of Fluids and Structures 141 (2026) 104490

Contents lists available at ScienceDirect

Journal of Fluids and Structures

journal homepage: www.elsevier.com/locate/jfs

Control of the channel flow past a cylinder by a piezo-actuated flexible splitter plate

Simone Cruciani [a,b], Franco Auteri [b], Michel Fournié [a,*]

[a] Fédération ENAC ISAE-SUPAERO ONERA, Université de Toulouse, Département d'Ingénierie des Systèmes Complexes (DISC), 10 Av. Edouard Belin, Toulouse, 31055, France

[b] Politecnico di Milano, Dipartimento di Scienze e Tecnologie Aerospaziali (DAER), Via La Masa 34, Milano, 20156, Italy

ARTICLE INFO

Keywords:
Optimal control
Fluid structure interaction
Arbitrary Lagrangian Eulerian
Reduced order model
Macro-fiber composites

ABSTRACT

We study the numerical stabilization around an unstable steady solution of a typical fluid-structure interaction problem constituted by a circular cylinder with a flexible splitter plate (Turek and Hron, 2006) actuated by piezoelectric devices and immersed in a fully developed, laminar channel flow. We define a linear feedback control that can locally stabilize the fully coupled non-linear system. The feedback is based on a spectral decomposition of a non-standard Differential Algebraic Equation resulting from a monolithic Arbitrary Lagrangian Eulerian Finite Element formulation where a simple model of the piezoelectric patches is considered. By projecting the full system on its unstable subspace, a Reduced Order Model is defined. The design of the controlled system exploits the computation of the unstable direct and adjoint subspaces to identify the number and distribution of the patches on the beam. Moreover, the feasibility of such a controller for a real application is assessed by looking at the saturation limit of the control input. This paper is an extension of the methodology presented in Airiau et al. (2017) and Fournié et al. (2019) to control the Navier-Stokes equations to a fluid-structure model actuated by macro-fiber composites. To our knowledge, such active controls are original and the numerical tests presented validate their promising potential.

1. Introduction

The interest in fluid-structure interaction (FSI) and control has been steadily increasing for the last decades by virtue of a large variety of application fields such as energy harvesting (Soti et al., 2017) or aeroelastic control for biomimetic propulsion for micro air vehicles (Moreno et al., 2023). The possibility to morph the shape of an aerodynamic surface adapting a wing for different flight conditions or the aim to control the flow by the deformation of the structure is a topic of high interest for the aeronautical industry (Bilgen et al., 2011). To achieve such an ability, the usage of smart materials in the control of the shape of an aerodynamic surface is assuming a growing interest. Indeed, smart materials are widely spreading in several applications because of their small size and reduced weight with respect to the most traditional mechanical or hydraulic actuators (Sun et al., 2016). Smart materials are, in general, structural materials that have also the ability to interact with the surrounding environment as actuators or transducers. Among them, piezoelectric materials, in particular *macro-fiber composites* (MFC), have been utilized in the aerospace industry for flow control, vibration suppression and noise reduction ('NASA Invention of the Year' Controls Noise and Vibration, 2007). The piezoelectric patches can be used exploiting either the *direct* or the *inverse* piezoelectric effect. Namely, once the piezoelectric structure

* Corresponding author.
E-mail address: michel.fournie@isae-supaero.fr (M. Fournié).

https://doi.org/10.1016/j.jfluidstructs.2025.104490
Received 9 March 2025; Received in revised form 8 October 2025; Accepted 11 December 2025
Available online 23 December 2025

is subjected to a mechanical stress, it produces an electric charge on the electrodes. This is the *direct* effect and by virtue of such behavior, sensors based on the measurements of the electric charge have been developed. It is also possible to extract energy from a vibrating piezoelectric structure in an energy harvester (Abdelkefi, 2015). Alternatively, a patch can be electrically charged to induce a mechanical stress. This is the *inverse* effect that is exploited in piezoelectric actuators. The number of applications of MFC in the aerospace industry is increasing because of their high bandwidth, flexible application and of the relatively large strains they can ensure (Smart Material website, n.d.). Moreover, the easy installation and the wide spectrum of applicability make them competitive with respect to other flow control techniques such as blowing and suction that lead to very complicated implementations. For instance, the possibility to control a small Unmanned Aerial Vehicule (UAV) equipped with MFC has been successfully tested in Bilgen et al. (2011) both numerically and experimentally, including flight tests. A variable-camber airfoil actuated by piezoelectric composites has been proposed in Bilgen and Friswell (2014). Another notable application for MFC is the vibration control of helicopters, as reported by Monner et al. (2011). The ability of MFC actuators to modify the trailing edge of an airfoil and its impact on the airfoil performance has also been investigated experimentally by many authors, see for instance Auteri et al. (2021), where simple scaling laws are formulated to model the effect of MFC actuators on the aerodynamic coefficients of an airfoil. They observed that the simplicity of installation of these actuators on an existing wing can represent an advantage for their usage with respect to other morphing techniques. However, they also discussed the experimental challenges of properly installing the actuators, for instance highlighting the fact that an imperfect gluing of the actuator can reduce significantly the actuator performance. Moreover, the high voltage required by these actuators, in the order of several hundred volts, represents a challenge for its installation on an aircraft.

In this paper, we numerically investigate the feasibility of controlling the flow field past a circular cylinder by a series of piezoelectric patches placed on a flexible plate clamped on the rear part of the cylinder. Such problem is a well known benchmark for FSI (Turek and Hron, 2006) but the control of the vortex street by the flexible appendage has not been investigated in great detail. An open loop control of this flow has been performed in Russo et al. (2020) based on a plasma discharge actuation model. They used a tangential velocity boundary condition in the region close to the separation point on the rigid cylinder surface and they changed its amplitude and its frequency. They observed that oscillations can be suppressed modifying the flow separation and they evaluated the control performance in terms of drag reduction and vibration reduction. In the present work, we study the numerical stabilization around an unstable steady solution of the aforementioned FSI problem (Turek and Hron, 2006), actuated by piezoelectric devices. The actuation mechanism exploits couples of piezoelectric patches that are used to induce a structural deformation by virtue of the electro-mechanical properties of the material. A simplified model of the piezoelectric patches is considered to include them in the Finite Element (FE) formulation. A closed-loop feedback controller is built to stabilize the unstable spectrum, recovering a stable steady state from an unstable equilibrium, suppressing the vortex shedding and the structural vibrations. The feedback is based on a spectral decomposition of a non-standard Differential Algebraic Equation (DAE) resulting from a monolithic Arbitrary Lagrangian Eulerian (ALE) Finite Element formulation. The linearized, semi-discrete system is reformulated in the classical Linear Time Invariant (LTI) system notation by eliminating the singular mass matrix through a new oblique projector. By projecting the complete system onto its unstable subspace, a Reduced Order Model (ROM) is constructed. The control design leverages the solution of a low-dimensional Algebraic Riccati Equation (ARE) formulated on the ROM, which is used exclusively for the regulator construction. The controlled system design utilizes the computation of both the unstable direct and adjoint subspaces to determine the number and placement of the patches along the beam. The feasibility of such a controller for a real application is assessed by looking at the saturation limit of the control input. This work represents a first step towards a feasible, easily implementable control for FSI configurations. Its current limitation for a real application is related to the still ideal *full state feedback* controller. Indeed, the knowledge of the *full state* of the system cannot be available and an estimation of it must be given by using just partial information. Therefore, a step towards a real application needs to take into account the estimation problem, designing a controller based on partial measurements as pressure sensors on the boundaries or piezoelectric sensors for the structural deformation. Moreover, the design of a robust controller, taking into account the inaccuracies and simplifications of the model with respect to a real case, as well as noise and uncertainties in the actuation system, would represent an improvement of the present work in the development of an implementable controller. The present work is an extension of the work Airiau et al. (2017) on the control of the Navier–Stokes equations by suction and blowing and of Fournié et al. (2019) on the control of the Navier–Stokes equations coupled with two independent beams governed by the one-dimensional Euler-Bernoulli damped equations. In Fournié et al. (2019), the end of the structure is fixed contrary to the present work, and the control is a force distributed along the structure.

The paper is organized as follows. In Section 2, we provide the numerical FSI model with details about the actuation mechanism and its implementation in the FE formulation. In Section 3, we formulate the optimal control problem and the Reduced Order Model. In Section 4, we provide the numerical results, focusing on the design choices made. An investigation on the role of the actuator location, the design parameters and the effect of the perturbation amplitude is performed. In Section 5, we summarize the main conclusions and innovation of this paper. In the Appendices, we provide the convergence analysis with respect to the spatial and temporal discretization, we report the mathematical steps to define the new oblique projector and we discuss about the role of the Reynolds number and the Young's modulus in the control of this FSI case.

2. Fluid-structure interaction with MFC actuators

2.1. Fluid-structure model

The FSI system treated with the ALE approach consists of three different sub-problems for the structure, defined by the state variable $\boldsymbol{q}_s$, the flow, defined by the state variable $\boldsymbol{q}_f$, and the domain deformation, with state variable $\boldsymbol{q}_e$. Here $\boldsymbol{q}_s$ denotes the

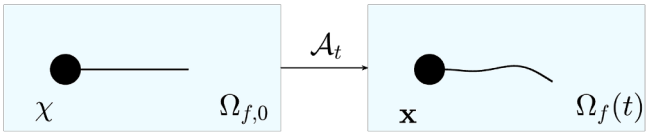

Fig. 1. ALE mapping $\mathcal{A}_t$ from the reference configuration $\Omega_{f,0}$ to the deformed configuration $\Omega_f(t)$ at time t.

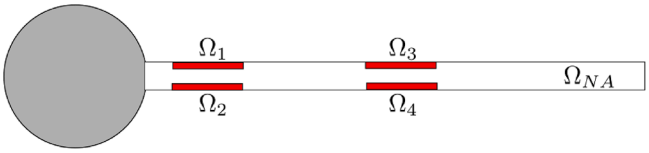

Fig. 2. Example of Ω_s definition. Non-actuated region: Ω_{NA} (white); actuated region: $\Omega_p = \bigcup_{n=1}^{N_p} \Omega_n$ (red). (For interpretation of the references to colour in this figure legend, the reader is referred to the web version of this article.).

displacement of the structure $\boldsymbol{s}$ and $\boldsymbol{u_s}$ is its velocity:

$$\boldsymbol{q_s} = \{\boldsymbol{s}, \boldsymbol{u_s}\}. \tag{1}$$

The flow state contains the fluid velocity $\boldsymbol{u}$, the reduced pressure p and the multiplier for the fluid-structure interface stress term λ_{fs}, used to ensure the continuity of the velocity on the FSI interface between the structure and the fluid on Γ_{fs}:

$$\boldsymbol{q_f} = \{\boldsymbol{u}, p, \lambda_{fs}\}. \tag{2}$$

The domain state describes the deformation of the fluid domain and includes the domain displacement $\boldsymbol{\xi}$ and the *pseudo* stress multiplier λ_e to enforce the continuity of the displacement between the solid domain and the fluid domain on Γ_{fs}:

$$\boldsymbol{q_e} = \{\boldsymbol{\xi}, \lambda_e\}. \tag{3}$$

The incompressible Navier-Stokes equations (INSE) describe the flow field in the time dependent fluid domain $\Omega_f(t)$:

$$\frac{\partial \boldsymbol{u}}{\partial t} + (\boldsymbol{u} \cdot \nabla)\boldsymbol{u} = -\nabla p + \frac{1}{Re}\Delta \boldsymbol{u}, \quad \nabla \cdot \boldsymbol{u} = 0. \tag{4}$$

The equations have been made dimensionless by a reference velocity $\hat{U}_\infty$, a length $\hat{L}_r$ and the fluid density $\hat{\rho}_f$ that define the dimensionless Reynolds number: $Re = \hat{\rho}_f \hat{U}_\infty \hat{L}_r \hat{\mu}_f^{-1}$, where $\hat{\mu}_f$ is the dynamic fluid viscosity. In the manuscript, we use the notation $\hat{}$ to denote dimensional quantities. In the present work, $\hat{U}_\infty$ is the average fluid velocity at the inlet and $\hat{L}_r$ is the cylinder diameter. As done in Pfister et al. (2019) and Pedraglio (2015), we write the equations in a fixed, reference configuration $\Omega_0 = \Omega_{f,0} \cup \Omega_{s,0}$ with the ALE strategy. Therefore, the INSE (4) are rewritten in a reference configuration using the mapping $\mathcal{A}_t$ that transforms the point χ in the reference undeformed configuration $\Omega_{f,0}$ into the point $\mathbf{x}$ in the deformed configuration $\Omega_f(t)$, as shown in Fig. 1. Namely:

$$\mathcal{A}_t : \begin{cases} \Omega_{f,0} & \longrightarrow & \Omega_f(t), \\ \chi & \longrightarrow & \mathbf{x}(t) = \chi + \xi(\chi, t), \end{cases} \tag{5}$$

where $\xi(\chi, t)$ is the fluid domain displacement at time t.

The fluid domain displacement ξ is computed solving the displacement extension problem:

$$\Delta \xi = 0 \qquad \text{in } \Omega_{f,0}, \tag{6}$$

with the boundary conditions enforcing the domain displacement on the flexible surface to be equal to the structural displacement along the interface Γ_{fs} and to be null on the outer boundaries of the channel and on the rigid surfaces. The structure behaviour of an isotropic material governed by the elasticity equation with Young's modulus $\hat{E}$ and Poisson's ratio ν. For the sake of clarity, we subdivided the structural domain Ω_s in a non-actuated region Ω_{NA} and an actuated region $\Omega_P = \bigcup_{n=1}^{N_P} \Omega_n$, where each *n-th* piezoelectric patch is located as shown in Fig. 2.

Hence, for a generic time t, $\Omega_s(t) = \Omega_{NA}(t) \cup \Omega_P(t)$. The same holds in the reference configuration, where we can partition the structural domain as $\Omega_{s,0} = \Omega_{NA,0} \cup \Omega_{P,0}$. We can extend the mapping $\mathcal{A}_t$ defined in (5) for the fluid domain to the structural domain. In $\Omega_s(t)$, each point is mapped from $\Omega_{s,0}$ by virtue of the transformation:

$$\mathcal{A}_t : \begin{cases} \Omega_{s,0} & \longrightarrow & \Omega_s(t) \\ \chi & \longrightarrow & \mathbf{x}(t) = \chi + s(\chi, t). \end{cases} \tag{7}$$

In the same manner as for the fluid, the equations for the structure are solved in a *stress-free* reference domain $\Omega_{s,0}$:

$$m^* \frac{\partial \boldsymbol{u_s}}{\partial t} = \nabla \cdot \mathbf{P}, \quad \frac{\partial \boldsymbol{s}}{\partial t} = \boldsymbol{u_s}, \tag{8}$$

where $\mathbf{P}$ is the first Piola-Kirchoff stress tensor. The elasticity Eq. (8) have been made dimensionless by the same reference quantities used for the INSE: $\hat{\rho}_f$, $\hat{U}_\infty$ and $\hat{L}_r$. Then, we can introduce the dimensionless mass ratio m^* and the dimensionless Young's modulus E:

$$m^* = \frac{\hat{\rho}_s}{\hat{\rho}_f}, \quad \text{and} \quad E = \frac{\hat{E}}{\hat{\rho}_f \hat{U}_\infty^2}, \tag{9}$$

where $\hat{\rho}_s$ is the solid density. A hyperelastic Saint Venant-Kirchoff structure model describes the relationship between the deformations and the stresses in the material Ω_{NA}. In the actuated region Ω_P, the same structural model has been employed. However, the additional strain due to the actuation effect has to be modelled, as described in Section 2.2. From the Saint Venant-Kirchoff model, we can write $\mathbf{P}$ as a function of the second Piola-Kirchoff stress tensor $\mathbf{S} = \lambda_1 tr(\mathbf{E})\mathbf{I} + 2\lambda_2\mathbf{E}$, where $\mathbf{E} = \frac{1}{2}(\nabla_\chi \boldsymbol{s} + (\nabla_\chi \boldsymbol{s})^T + (\nabla_\chi \boldsymbol{s})^T \nabla_\chi \boldsymbol{s})$ is the Lagrangian Green strain tensor and $\lambda_1 = \frac{E\nu}{(1+\nu)(1-2\nu)}$, $\lambda_2 = \frac{E}{2(1+\nu)}$ are the Lamé coefficients of the material (in dimensionless form). In particular, $\mathbf{P} = \mathbb{J}_{\mathcal{A}_t}\mathbf{S}$, where $\mathbb{J}_{\mathcal{A}_t} = \mathbf{I} + \nabla_\chi \mathbf{s}$ is the deformation gradient in the structure. The notation ∇_χ is used here to denote the gradient of a vector field in the reference configuration. To sum up, the complete fluid-structure interaction model requires the solution of the following system of equations:

$$\begin{cases} \frac{\partial \boldsymbol{u}}{\partial t} + (\boldsymbol{u}\cdot\nabla)\boldsymbol{u} = -\nabla p + \frac{1}{Re}\Delta \boldsymbol{u}, \quad \nabla\cdot\boldsymbol{u} = 0 & \text{in } \Omega_f(t), \\ m^* \frac{\partial \boldsymbol{u}_s}{\partial t} = \nabla\cdot\mathbf{P}, \quad \frac{\partial \boldsymbol{s}}{\partial t} = \boldsymbol{u}_s & \text{in } \Omega_{s,0}, \\ \boldsymbol{s} = 0 \text{ on } \Gamma_c, \quad \boldsymbol{u} = \boldsymbol{u}_{in} \text{ on } \Gamma_{inlet}, \quad \boldsymbol{u} = 0 & \text{on } \Gamma_{wall}, \\ [-p\boldsymbol{I} + \frac{2}{Re}\mathbf{D}]\cdot\mathbf{n}_f = 0 & \text{on } \Gamma_{outlet}, \\ \boldsymbol{u} = \boldsymbol{u}_s,\ \boldsymbol{\xi} = \boldsymbol{s},\ [-p\boldsymbol{I} + \frac{2}{Re}\mathbf{D}]\cdot\mathbf{n}_f + \boldsymbol{\sigma}_s\cdot\mathbf{n}_s = 0 & \text{on } \Gamma_{fs}, \\ \Delta\boldsymbol{\xi} = 0 & \text{in } \Omega_{f,0}, \\ \boldsymbol{\xi} = 0 & \text{on } \partial\Omega_{f,0}\setminus\Gamma_{fs}, \end{cases} \tag{10}$$

where $\mathbf{D} = \frac{1}{2}(\nabla\boldsymbol{u} + \nabla\boldsymbol{u}^T)$ is the symmetric part of the rate-of-strain tensor and $\boldsymbol{\sigma}_s$ is the Cauchy stress tensor for the structure that satisfies the relation $\boldsymbol{\sigma}_s = \frac{1}{J}\mathbf{P}\mathbb{J}_{\mathcal{A}_t}^T$, where $J = \det(\mathbb{J}_{\mathcal{A}_t})$. Moreover, $\mathbf{n}_f$ and $\mathbf{n}_s$ are the normal unit vectors pointing outwards from the fluid and the solid domain, respectively, which satisfy $\mathbf{n}_f = -\mathbf{n}_s = \mathbf{n}$. The continuity of the normal component of the stress tensor can be stated as:

$$[-p\boldsymbol{I} + \frac{2}{Re}\mathbf{D}]\cdot\mathbf{n} = \boldsymbol{\sigma}_s\cdot\mathbf{n} = \boldsymbol{\lambda}_{\boldsymbol{fs}} \qquad \text{on } \Gamma_{fs}. \tag{11}$$

In (10), the governing equations for the fluid are supplemented by Dirichlet boundary conditions for the velocity at the inlet surface Γ_{inlet} and on the rigid walls Γ_{wall}, while a *stress-free* boundary condition is enforced at the outlet Γ_{outlet}. The structural displacement is set to zero on the clamped side Γ_c of the plate and the fluid domain displacement is set to zero on the boundaries of the fluid domain with the exception of the fluid-structure interface Γ_{fs}. On this interface, the continuity of the velocity, of the normal stress and of the displacement are enforced. Note that the fluid equations and the boundary conditions on the fluid-structure interface (11) are written in the deformed configuration, for brevity. However, their numerical solution is performed in the reference configuration, as in Pfister et al. (2019).

2.2. MFC Model

The voltage applied on the actuator electrodes is the external input on the system and the control mechanism is based on an induced deformation of the piezoelectric patch due to it. For such reason, the induced deformation is the physical mechanism we have to model in the FE formulation. In order to do that, we follow the approach proposed in Carini et al. (2017) and Thomas et al. (2009). We proceed by introducing the governing equations and the constitutive relations for a piezoelectric material (IEEE Standard on Piezoelectricity, n.d.). Then, we introduce suitable hypotheses that allow us to simplify the electro-mechanical problem using only a few variables (in particular: the voltage difference applied to the electrodes of the MFC), as done in Thomas et al. (2009). In conclusion, we derive the weak formulation of the control term to be able to use it in the FE method. This is a simplified model that allows one to easily embed MFC actuators in the current FE formulation. No electrical circuit components, actuation uncertainties or delays that characterise real applications have been modelled here.

2.2.1. Governing equation

Let us consider the domain Ω_n of the *n-th* piezoelectric patch at equilibrium. Linear elasticity (8) governs the structural displacement of the piezoelectric structure. We use the same hyperelastic structural model for both the structure and the piezoelectric patch. The piezoelectric constitutive equations (IEEE Standard on Piezoelectricity, n.d.) provide the effect of the electric field $\boldsymbol{f}$ on the patch:

$$\mathbf{S}_{ij} = c_{ijkl}\mathbf{E}_{kl} - l_{kij}\boldsymbol{f}_k. \tag{12}$$

With a compressed notation (Côté et al., 2004; IEEE Standard on Piezoelectricity, n.d.), we can retrieve a matrix form relation $\mathbf{S} = \mathbf{C}\mathbf{E} - \mathbf{L}^T\boldsymbol{f}$, which is commonly written in the following way $\mathbf{S} = \mathbf{C}(\mathbf{E} - \mathbf{F}^T\boldsymbol{f})$, with $\mathbf{L}^T = \mathbf{C}\mathbf{F}^T$. The term $\boldsymbol{E}_{\boldsymbol{act}} = -\mathbf{F}^T\boldsymbol{f}$ represents the induced deformation due to the electric field inside the actuator. This is a common way to write the piezoelectric constitutive equations because the MFC manufacturers usually provide the $\mathbf{F}$ coefficients that relate the induced deformation of the patch to the

electrical field inside the MFC. We can note that the piezoelectric actuation model is equivalent to a thermal stress. The thermal stress analogy has been widely used in the literature to model the MFC actuation inside a FE model, see for instance Côté et al. (2004). The only difference is that, for the piezoelectric actuators, the induced deformation depends on the electrical field inside the MFC, hence on the applied electric voltage, and not on the temperature.

2.2.2. Simplifying hypotheses

Material properties. We need to specify the structural properties of the piezoelectric patch. A simple way to do it is to consider an isotropic material and use the relative constitutive equations:

$$\mathbf{S}_{ij} = \lambda_1 \bar{\mathbf{E}}_{kk} \boldsymbol{I}_{ij} + 2\lambda_2 \bar{\mathbf{E}}_{ij}, \tag{13}$$

where λ_1 and λ_2 are the Lamé coefficients of the material and $\bar{\mathbf{E}} = \mathbf{E} + \mathbf{E}_{\mathbf{act}}$ is the Lagrangian strain tensor with the additional induced deformation caused by the *inverse* piezoelectric effect. We consider the same material in both the splitter plate and the patches. In this case, both the Poisson ratio and the Young's modulus are constant inside the structure as well as the Lamé coefficients.

Piezoelectric induced deformation. The induced deformation that is used as actuation to deform the structure remains to be specified. In general, the induced deformation tensor due to the electrical field applied to the piezoelectric patch is $\mathbf{E}_{\mathbf{act}} = -\mathbf{F}^T \boldsymbol{f}$, but we can use simplified formulations taking into account the type of MFC patch. Different actuators have been developed, some of them can induce shear strain and other ones can twist the structure. We are interested in MFC that induce an axial strain in the structure and we use couples of patches, with one MFC placed on the top of the structure and the other one on the bottom (as shown, for example, in Fig. 2). This setup allows us to induce a bending deformation in the plate when they are actuated with an opposite voltage difference. The piezoelectric strain tensor due to the actuation $\mathbf{E}_{\mathbf{act}}$ has a single non-zero entry that is the axial strain $E_{act_{xx}}$. In particular, from the data-sheets (see for example Smart Material website (n.d.)) we used the average free-strain per volt coefficient $\hat{\alpha}$ to relate the axial induced strain only to the applied voltage. The free-strain per unit voltage has physical dimension [1/V]. To recover a dimensionless equation, we use the maximum applicable voltage $\hat{V}_{max}$ as reference and we can write $E_{act_{xx}} = \hat{\alpha}\Delta\hat{V} = \hat{\alpha}\hat{V}_{max}\Delta V = \alpha\Delta V$, where $\alpha = \hat{\alpha}\hat{V}_{max}$ is the dimensionless free-strain per volt and ΔV is the dimensionless applied voltage, that is the control input parameter of the system under consideration. In general, the MFC voltage range is not symmetrical with respect to a null applied voltage $\Delta\hat{V} \in [\hat{V}_{low}, \hat{V}_{high}]$. We use $\hat{V}_{max} = \min(\hat{V}_{high}, -\hat{V}_{low})$. In this way we can easily check if the control exceeds the actuator limit, namely if $|\Delta V| > 1.0$.

2.3. Semidiscrete system and introduction of the control

Adopting a spatial discretization for both the fluid and the structural domain and defining a finite element space for all the variables, the FE discretization of the weak formulation for the three sub-problems leads to the following nonlinear, monolithic system in $\Omega_0 = \Omega_{s,0} \cup \Omega_{f,0}$:

$$M_{nl}(\boldsymbol{q})\dot{\boldsymbol{q}} = A_{nl}(\boldsymbol{q}) + B(\boldsymbol{q})\mathbf{u}_{ctrl}, \tag{14}$$

where $\boldsymbol{q} = (\boldsymbol{q_s}, \boldsymbol{q_f}, \boldsymbol{q_e})$ is the state variable of size N, $\dot{\boldsymbol{q}}$ is its time derivative and

$$\mathbf{u}_{ctrl} = (\Delta V_1, \cdots, \Delta V_{N_p}) \tag{15}$$

is the control input vector where N_p is the number of patches considered and ΔV_i is the dimensionless voltage difference applied on the i-th actuator. Let us remark here that the control operator B has non-zero values only in the linear elasticity equation. This is due to the fact that the actuation forces only the structure. Moreover, such operator has non-zero contributions only for the degrees of freedom which are inside the piezoelectric domain. Indeed, B is obtained by integrating the induced deformation effect on the actuator patches using the linear elasticity Eq. (8), the constitutive equation of the material (13) and the piezoelectric actuation model $E_{act_{xx}} = \alpha\Delta V$. The only boundary terms that contribute to the weak formulation of (8) on the domain of each patch are those on the fluid-structure interface. Notice that the boundary terms on the interface between each patch and the surrounding non-actuated region cancel out. Finally, we can define the control matrix for the *n-th* actuator patch in the domain $\Omega_{n,0}$, associated to the structural velocity test function δu_{s_i}, by:

$$B^n = -\int_{\Omega_{n,0}} \frac{\partial \delta u_{s_i}}{\partial x_j} [\mathbb{J}_{\mathcal{A}_t}]_{il} \left(\lambda_1 \alpha \boldsymbol{I}_{lj} + 2\lambda_2 \begin{bmatrix} \alpha & 0 \\ 0 & 0 \end{bmatrix}_{lj} \right) d\Omega_{n,0}. \tag{16}$$

3. Optimal feedback controller

The controller is based on the Linear Quadratic Regulator (LQR) theory. Starting from the linearization of the nonlinear system (14) about a steady state solution $\bar{\boldsymbol{q}}$ computed when no control inputs are imposed, we consider the problem:

$$M\,\dot{\boldsymbol{q}} = A\,\boldsymbol{q} + B\,\mathbf{u}_{ctrl}. \tag{17}$$

An optimal feedback regulator is computed minimizing a quadratic cost function that takes into account the error with respect to the desired solution and the control effort we need to spend on it. The cost function we consider is defined as:

$$J(\mathbf{u}_{ctrl}) = \frac{1}{2}\int_0^\infty [\mathbf{u}_{ctrl}(t)^T\, R\, \mathbf{u}_{ctrl}(t) + \mathbf{e}_{\boldsymbol{q}}(t)^T Q\, \mathbf{e}_{\boldsymbol{q}}(t)]dt, \tag{18}$$

with $\mathbf{e}_q(t) = \boldsymbol{q}(t) - \bar{\boldsymbol{q}}$. The matrices R and Q are weighting terms for the control input and the error with respect to the steady solution, respectively. Moreover, Q is the symmetric positive semi-definite weight matrix for the error, and R is the symmetric positive definite control weight matrix. The control matrix Q can be null, then a degenerate Riccati equation is obtained (Kesavan and Raymond, 2009). Solving an Algebraic Riccati Equation (ARE), we obtain an optimal regulator that stabilizes the closed-loop system. Due to the high computational cost of the ARE solution, the control problem is formulated on a Reduced Order Model (ROM). This allows us to solve very cheaply the ARE focusing only on the stabilization of the unstable dynamics. In order to do that, we firstly write the FSI system in a controllable formulation, then we project the full system on the subspace of the unstable dynamics. Finally, the control for the full system is deduced from the ROM.

3.1. Formulation of the system in classical controllable framework

To represent the problem in the classical formulation where the theory can be applied, we follow the strategy used for the Navier–Stokes system based on the Leray projector in Raymond (2006). Using the same notation as in Airiau et al. (2017), we can collect all the multipliers in a variable $\boldsymbol{\eta}$ and the remaining variables in a vector $\mathbf{z}$ of dimension $N_{\mathbf{z}}$. The equation for the fluid domain is treated separately with its own state $\boldsymbol{q}_e$. With the following notations:

$$\mathbf{z} = \{s, \boldsymbol{u}_s, \boldsymbol{u}\} \quad \text{and} \quad \boldsymbol{\eta} = \{p, \lambda_{fs}\},$$

the linearized, semidiscrete system (17) can be formulated in the following form (using the same notation for the matrices M, A, B after reordering):

$$M \frac{d}{dt}\begin{pmatrix} \mathbf{z} \\ \boldsymbol{\eta} \\ \boldsymbol{q}_e \end{pmatrix} = A \begin{pmatrix} \mathbf{z} \\ \boldsymbol{\eta} \\ \boldsymbol{q}_e \end{pmatrix} + B\, \mathbf{u}_{ctrl}. \tag{19}$$

It is convenient to collect some blocks of the mass matrix that can be written in the following form:

$$M = \begin{bmatrix} M_{\mathbf{zz}} & 0 & M_{\mathbf{zq}_e} \\ 0 & 0 & 0 \\ 0 & 0 & 0 \end{bmatrix}, \tag{20}$$

where (ξ being the fluid domain displacement, see (5)):

$$M_{\mathbf{zz}} = \begin{bmatrix} M_{ss} & 0 & 0 \\ 0 & M_{u_s u_s} & 0 \\ 0 & 0 & M_{uu} \end{bmatrix} \quad \text{and} \quad M_{\mathbf{zq}_e} = \begin{bmatrix} 0 & 0 \\ 0 & 0 \\ M_{u\xi} & 0 \end{bmatrix}.$$

In the same way, we can collect each block of the matrix A:

$$A = \begin{bmatrix} A_{\mathbf{zz}} & A_{\mathbf{z}\eta} & A_{\mathbf{z}q_e} \\ A_{\mathbf{z}\eta}^T & 0 & A_{\eta q_e} \\ A_{q_e \mathbf{z}} & 0 & A_{q_e q_e} \end{bmatrix},$$

and for B, we use the sub-matrix B^n defined in (16) associated to the n-th patch:

$$B = \begin{bmatrix} B^1 \dots B^{N_p} \end{bmatrix} = \begin{bmatrix} B_{\mathbf{z}}^1 \dots B_{\mathbf{z}}^{N_p} \\ 0 \quad \dots \quad 0 \\ 0 \quad \dots \quad 0 \end{bmatrix} = \begin{bmatrix} B_{\mathbf{z}} \\ 0 \\ 0 \end{bmatrix}. \tag{21}$$

Here $B_{\mathbf{z}}$ has non-zero entries only in the elasticity equation:

$$B_{\mathbf{z}} = \begin{bmatrix} 0 \\ B_{u_s} \\ 0 \end{bmatrix}. \tag{22}$$

In order to formulate the linearized system (19) in the classical controllable formulation, we first eliminate the fluid domain variables $\boldsymbol{q}_e$ defined in (3) from the system and then build an ad-hoc projector to eliminate the multipliers. We prove that these manipulations have no effect on the solution of the eigenvalue problem used to define the control.

3.1.1. Eliminating the fluid domain variables

In order to rewrite the system in the controlled form, the first step is to remove the fluid domain displacement from the equations. From the last equation in (19), we can compute explicitly the fluid domain state $\boldsymbol{q}_e$:

$$\boldsymbol{q}_e = -A_{q_e q_e}^{-1} A_{q_e \mathbf{z}} \mathbf{z}. \tag{23}$$

The invertibility of the matrix $A_{q_e q_e}$ follows from the fact that the matrix

$$A_{q_e q_e} = \begin{bmatrix} A_{\xi\xi} & A_{\xi\lambda_e} \\ A_{\xi\lambda_e}^T & 0 \end{bmatrix},$$

is a block, anti-diagonal matrix and hence invertible as soon as $A_{\xi\lambda_e}$ has full rank which is ensured by our choice of finite elements for the multiplier to satisfy the well-known inf-sup condition (Babuška, 1973; Brezzi, 1974). If we plug (23) into (19), we obtain:

$$\begin{bmatrix} \tilde{M}_{\mathbf{zz}} & 0 \\ 0 & 0 \end{bmatrix} \frac{d}{dt}\begin{pmatrix} \mathbf{z} \\ \boldsymbol{\eta} \end{pmatrix} = \begin{bmatrix} A_{\mathbf{zz}} - A_{\mathbf{z}q_e} A_{q_eq_e}^{-1} A_{q_e\mathbf{z}} & A_{\mathbf{z}\eta} \\ A_{\mathbf{z}\eta}^T - A_{\eta q_e} A_{q_eq_e}^{-1} A_{q_e\mathbf{z}} & 0 \end{bmatrix} \begin{pmatrix} \mathbf{z} \\ \boldsymbol{\eta} \end{pmatrix} + \begin{bmatrix} B_{\mathbf{z}} \\ 0 \end{bmatrix} \mathbf{u}_{ctrl}, \tag{24}$$

where $\tilde{M}_{\mathbf{zz}} = M_{\mathbf{zz}} - M_{\mathbf{z}q_e} A_{q_eq_e}^{-1} A_{q_e\mathbf{z}}$ is the non-zero block of the mass matrix of the system, once the fluid domain variables have been removed. We can introduce the following notation to write the Eq. (24) as:

$$\tilde{M}\, \frac{d}{dt}\begin{pmatrix} \mathbf{z} \\ \boldsymbol{\eta} \end{pmatrix} = \tilde{A}\begin{pmatrix} \mathbf{z} \\ \boldsymbol{\eta} \end{pmatrix} + \tilde{B}\, \mathbf{u}_{ctrl}, \tag{25}$$

where $\tilde{}$ expresses the modified system, obtained from the initial one (19) removing the fluid domain variables.

3.1.2. Projected system. Elimination of the multipliers

Now, we can perform similar steps as those made in Airiau et al. (2017), and build an oblique projector Π^T onto $\mathrm{Ker}(\tilde{\mathrm{A}}_{\mathbf{z}\eta}^{\mathrm{T}})$ parallel to $\mathrm{Im}(\tilde{\mathrm{M}}_{\mathbf{zz}}^{-1}\mathrm{A}_{\mathbf{z}\eta})$, with $\tilde{A}_{\mathbf{z}\eta}^T = A_{\mathbf{z}\eta}^T - A_{\eta q_e} A_{q_eq_e}^{-1} A_{q_e\mathbf{z}}$. All the steps that lead to the definition of the oblique projector in the present case of FSI are shown in the Appendix B. The projector is defined as:

$$\Pi^T = I - \tilde{M}_{\mathbf{zz}}^{-1} A_{\mathbf{z}\eta}\left[\tilde{A}_{\mathbf{z}\eta}^T \tilde{M}_{\mathbf{zz}}^{-1} A_{\mathbf{z}\eta}\right]^{-1} \tilde{A}_{\mathbf{z}\eta}^T. \tag{26}$$

The projected version of system (24) is:

$$\Pi^T \dot{\mathbf{z}} = \Pi^T \tilde{M}_{\mathbf{zz}}^{-1} \tilde{A}_{\mathbf{zz}}\mathbf{z} + \Pi^T \tilde{M}_{\mathbf{zz}}^{-1} B_{\mathbf{z}} \mathbf{u}_{ctrl}, \tag{27}$$

where $\tilde{A}_{\mathbf{zz}} = A_{\mathbf{zz}} - A_{\mathbf{z}q_e} A_{q_eq_e}^{-1} A_{q_e\mathbf{z}}$, that is equivalent to:

$$\Pi^T \dot{\mathbf{z}} = \boldsymbol{A}\Pi^T \mathbf{z} + \boldsymbol{A}(I - \Pi^T)\mathbf{z} + \boldsymbol{B}\mathbf{u}_{ctrl}, \tag{28}$$

where $\boldsymbol{A} = \Pi^T \tilde{M}_{\mathbf{zz}}^{-1} \tilde{A}_{\mathbf{zz}}$, $\boldsymbol{B} = \Pi^T \tilde{M}_{\mathbf{zz}}^{-1} B_{\mathbf{z}}$ with $B_{\mathbf{z}}$ defined in (21). In this case, the elimination of the fluid domain variables does not affect at all the control because the control is localized on the structure (22) and it forces only the structural equation without any contribution from the fluid domain variables. The projected system can be simplified because $(I - \Pi^T)\mathbf{z} = 0$ from the second row in (24). Recovering the definition of Π^T in (26) and that of $\tilde{A}_{\mathbf{z}\eta}^T$, we obtain a system for $\Pi^T\mathbf{z}$, given by:

$$\Pi^T \dot{\mathbf{z}} = \boldsymbol{A}\Pi^T \mathbf{z} + \boldsymbol{B}\mathbf{u}_{ctrl}. \tag{29}$$

3.2. Control design

The same steps performed for the Navier-Stokes system in Airiau et al. (2017) can be used on the controlled system described by the pair $(\boldsymbol{A}, \boldsymbol{B})$ in the variable $\Pi^T\mathbf{z}$. We determine the feedback control law based on a spectral decomposition of the dynamical system. We prove relationships between the eigenvalue problems associated to (29) for $\mathbf{z}$ only, to (25) for $(\mathbf{z}, \boldsymbol{\eta})$ and to (19) for the variables $(\mathbf{z}, \boldsymbol{\eta}, \boldsymbol{q}_e)$. These properties are crucial to avoid assembling the projector (26) to define the feedback associated to (29). This original result is an extension of Airiau et al. (2017) when the ALE approach is used in the FSI framework.

3.2.1. Eigenvalue problems

A pair $(\lambda, \mathbf{v}) \in \mathbb{C}^* \times \mathbb{C}^{N_{\mathbf{z}}}$, $\mathbf{v} \in \mathrm{Ker}(\tilde{\mathrm{A}}_{\mathbf{z}\eta}^{\mathrm{T}}) = \mathrm{Im}(\Pi^{\mathrm{T}})$, $\mathbf{v} \neq 0_{\mathbb{C}^{N_{\mathbf{z}}}}$ is a solution of the eigenvalue problem (EVP)

$$\lambda\mathbf{v} = \boldsymbol{A}\mathbf{v} \tag{30}$$

if and only if $(\lambda, \mathbf{v}, \boldsymbol{\eta}_{\mathbf{v}})$, with

$$\boldsymbol{\eta}_{\mathbf{v}} = -\left[\tilde{A}_{\mathbf{z}\eta}^T \tilde{M}_{\mathbf{zz}}^{-1} A_{\mathbf{z}\eta}\right]^{-1} \tilde{A}_{\mathbf{z}\eta}^T \tilde{M}_{\mathbf{zz}}^{-1} \tilde{A}_{\mathbf{zz}}\mathbf{v}, \tag{31}$$

is a solution of the EVP for $(\lambda, \mathbf{v}, \boldsymbol{\eta}_{\mathbf{v}}) \in \mathbb{C}^* \times \mathbb{C}^{N_{\mathbf{z}}} \times \mathbb{C}^{N_{\eta}}$, $\mathbf{v} \neq 0_{\mathbb{C}^{N_{\mathbf{z}}}}$:

$$\lambda \tilde{M}\begin{bmatrix} \mathbf{v} \\ \boldsymbol{\eta}_{\mathbf{v}} \end{bmatrix} = \tilde{A}\begin{bmatrix} \mathbf{v} \\ \boldsymbol{\eta}_{\mathbf{v}} \end{bmatrix}. \tag{32}$$

The triplet $(\lambda, \mathbf{v}, \boldsymbol{\eta}_{\mathbf{v}})$ is solution of (31) and (32) if and only if $(\lambda, \mathbf{v}, \boldsymbol{\eta}_{\mathbf{v}}, \boldsymbol{q}_{e\mathbf{v}})$, with

$$\boldsymbol{q}_{e\mathbf{v}} = -A_{q_eq_e}^{-1} A_{q_e\mathbf{z}}\mathbf{v}, \tag{33}$$

is a solution of the EVP for $(\lambda, \mathbf{v}, \boldsymbol{\eta}_{\mathbf{v}}, \boldsymbol{q}_{e\mathbf{v}}) \in \mathbb{C}^* \times \mathbb{C}^{N_{\mathbf{z}}} \times \mathbb{C}^{N_{\eta}} \times \mathbb{C}^{N_e}$, $\mathbf{v} \neq 0_{\mathbb{C}^{N_{\mathbf{z}}}}$:

$$\lambda M\begin{bmatrix} \mathbf{v} \\ \boldsymbol{\eta}_{\mathbf{v}} \\ \boldsymbol{q}_{e\mathbf{v}} \end{bmatrix} = A\begin{bmatrix} \mathbf{v} \\ \boldsymbol{\eta}_{\mathbf{v}} \\ \boldsymbol{q}_{e\mathbf{v}} \end{bmatrix}. \tag{34}$$

Proof In Appendix C.

3.2.2. Reduced order model (ROM)

We formulate the feedback control as a *state feedback* control assuming the *full state* is known. However, due to the large size of the discrete system, such approach requires a large amount of computational effort to be solved. A Reduced Order Model (ROM) is defined and the associated Riccati equation is derived and solved. Indeed, the Riccati equation obtained by this approach has small size and is therefore numerically tractable, while it would become computationally intractable for the full, high-dimensional system. In this spirit, the *full state feedback* controller stabilizing the unstable modes that form the ROM is designed, *once and for all*, *offline*, before the time marching simulation. It is subsequently applied in the time marching simulations of the full size, high-dimensional FSI system. We look for a decomposition of $\mathbb{R}^{N_\mathbf{z}}$ into a sum of the generalized eigenspaces of the operator $\boldsymbol{A}\Pi^T$. We start from the complex eigenvalue problems (30)–(34). Using a complex Jordan decomposition, we define two bases of $\mathbb{C}^{N_\mathbf{z}}$ constituted of the eigenvectors and generalized eigenvectors $(\boldsymbol{f}^1, \cdots, \boldsymbol{f}^{N_\mathbf{z}})$ and $(\boldsymbol{\phi}^1, \cdots, \boldsymbol{\phi}^{N_\mathbf{z}})$ of the problem (30) (on $\boldsymbol{A}$) and of its adjoint problem (on $\boldsymbol{A}^\#$), respectively. If we denote by $G_\mathbb{C}(\lambda_j)$ (resp. $G^*_\mathbb{C}(\lambda_j)$) the complex generalized eigenspace of $\boldsymbol{A}$ (resp. $\boldsymbol{A}^\#$) associated with λ_j, it is possible to deduce the real one by $G_\mathbb{R}(\lambda_j) = \Re(G_\mathbb{C}(\lambda_j)) \cup \Im(G_\mathbb{C}(\lambda_j))$ (resp. $G^*_\mathbb{R}(\lambda_j)$) that corresponds to the real basis $(\boldsymbol{e}^1, \cdots, \boldsymbol{e}^{N_\mathbf{z}})$ of $\mathbb{R}^{N_\mathbf{z}}$ (resp. $(\boldsymbol{\xi}^1, \cdots, \boldsymbol{\xi}^{N_\mathbf{z}})$). We have the following biorthogonality condition:

$$(\boldsymbol{e}^i)^T \tilde{\boldsymbol{M}}_{\mathbf{zz}} \boldsymbol{\xi}^j = \delta_{ij} \text{ for } 1 \leq i, j \leq N_\mathbf{z}.$$

We refer to Airiau et al. (2017) for more details. If we define the matrices $\boldsymbol{E} \in \mathbb{R}^{N_\mathbf{z} \times N_\mathbf{z}}$ whose columns are $(\boldsymbol{e}^1, \cdots, \boldsymbol{e}^{N_\mathbf{z}})$ and $\boldsymbol{\Xi} \in \mathbb{R}^{N_\mathbf{z} \times N_\mathbf{z}}$ whose columns are $(\boldsymbol{\xi}^1, \cdots, \boldsymbol{\xi}^{N_\mathbf{z}})$, we have:

$$\Lambda = \boldsymbol{E}^{-1} \boldsymbol{A} \Pi^T \boldsymbol{E},$$

where Λ is a decomposition of $\mathbf{A}$ into real Jordan blocks. For the direct eigenvalue problem, we define the unstable subspace:

$$\mathbb{Z}_u = \oplus_{j \in J_u} G_\mathbb{R}(\lambda_j) = \text{vect}\{\mathbf{e}^1, \cdots, \mathbf{e}^{d_u}\},$$

and for the adjoint eigenvalue problem:

$$\mathbb{Z}^*_u = \oplus_{j \in J_u} G^*_\mathbb{R}(\lambda_j) = \text{vect}\{\boldsymbol{\xi}^1, \cdots, \boldsymbol{\xi}^{d_u}\},$$

where J_u is a finite subset of $\mathbb{N}$ such that the family $(\lambda_j)_{j \in J_u}$ contains all the unstable eigenmodes of $\boldsymbol{A}$ and d_u is the dimension of $\mathbb{Z}_u$. In a same manner, we can define $\mathbb{Z}_s$ and $\mathbb{Z}^*_s$ such that

$$\mathbb{R}^{N_\mathbf{z}} = \mathbb{Z}_u \oplus \mathbb{Z}_s \oplus \mathbb{K},$$

where $\mathbb{K}$ contains the eigenvectors that generate $\text{Ker}(\boldsymbol{A}\Pi^T)$. We denote by $\boldsymbol{E}_u$ and $\boldsymbol{\Xi}_u$ in $\mathbb{R}^{N_\mathbf{z}}$, the matrices whose columns are $(\mathbf{e}^1, \cdots, \mathbf{e}^{d_u})$ and $(\boldsymbol{\xi}^1, \cdots, \boldsymbol{\xi}^{d_u})$ respectively. Then the direct and the adjoint problems can be written as:

$$\tilde{A}\begin{pmatrix} \boldsymbol{E_u} \\ \boldsymbol{E_{\eta,u}} \end{pmatrix} = \tilde{M}\begin{pmatrix} \boldsymbol{E_u} \\ \boldsymbol{E_{\eta,u}} \end{pmatrix}\Lambda_u \qquad \text{and} \qquad \tilde{A}^T\begin{pmatrix} \boldsymbol{\Xi_u} \\ \boldsymbol{\Xi_{\eta,u}} \end{pmatrix} = \tilde{M}^T\begin{pmatrix} \boldsymbol{\Xi_u} \\ \boldsymbol{\Xi_{\eta,u}} \end{pmatrix}\Lambda_u^T,$$

with $\Lambda_u = \boldsymbol{\Xi_u}^T \tilde{A}_{\mathbf{zz}} \boldsymbol{E_u}$. The operator $\boldsymbol{\pi_u} = \boldsymbol{E_u}\boldsymbol{\Xi_u}^T \tilde{\boldsymbol{M}}_{\mathbf{zz}} \in \mathcal{L}(\mathbb{R}^{N_\mathbf{z}}, \mathbb{Z}_u)$ is the projector onto $\mathbb{Z}_u$ parallel to $\mathbb{Z}_s \oplus \mathbb{K}$. Projecting the system (29) onto $\mathbb{Z}_u$ using $\boldsymbol{\pi_u}$, for $\boldsymbol{\zeta}_u(t)$ defined by $\boldsymbol{\zeta}_u(t) = \boldsymbol{\Xi}_u^T \tilde{\boldsymbol{M}}_{\mathbf{zz}}\, \mathbf{z}(t)$ and $\mathbb{B}_u = \boldsymbol{\Xi}_u^T \boldsymbol{B}_\mathbf{z}$ (see (21)), we have:

$$\boldsymbol{\zeta}'_u(t) = \Lambda_u\, \boldsymbol{\zeta}_u(t) + \mathbb{B}_u\, \mathbf{u}_{ctrl}, \quad \boldsymbol{\zeta}_u(0) = \boldsymbol{\Xi}_u^T \tilde{\boldsymbol{M}}_{\mathbf{zz}} \mathbf{z}_0. \tag{35}$$

To stabilize the system (17), it is sufficient to stabilize the equation satisfied by $\boldsymbol{\zeta}_u$ in (35) and then define a stabilizing feedback law $\mathbb{K}_u$ using the solution $\mathbb{P}_{\omega,u}$ of an Algebraic Riccati Equation. More precisely, for all $Q \in \mathcal{L}(\mathbb{R}^{d_u})$ satisfying $Q = Q^T \geq 0$ and a shift ω such that $-\omega < \Re(\text{spect}(\Lambda_u))$, the following Algebraic Riccati Equation:

$$\begin{aligned} &\mathbb{P}_{\omega,u} \in \mathcal{L}(\mathbb{R}^{d_u}),\ \mathbb{P}_{\omega,u} = \mathbb{P}^T_{\omega,u} \geq 0, \\ &\Lambda_u + \omega \boldsymbol{I}_{\mathbb{R}^{d_u}} - \mathbb{B}_u \mathbb{B}_u^T \mathbb{P}_{\omega,u} \text{ is stable}, \\ &\mathbb{P}_{\omega,u}(\Lambda_u + \omega \boldsymbol{I}_{\mathbb{R}^{d_u}}) + (\Lambda_u^T + \omega \boldsymbol{I}_{\mathbb{R}^{d_u}})\mathbb{P}_{\omega,u} - \mathbb{P}_{\omega,u}\, \mathbb{B}_u \mathbb{B}_u^T \mathbb{P}_{\omega,u} + Q = 0, \end{aligned} \tag{36}$$

admits a unique solution $\mathbb{P}_{\omega,u}$ and we define:

$$\mathbb{K}_u = -\mathbb{B}_u^T \mathbb{P}_{\omega,u}\, \boldsymbol{\Xi}_u^T \tilde{\boldsymbol{M}}_{\mathbf{zz}}. \tag{37}$$

The closed loop linear system (17) for $\mathbf{u}_{ctrl} = \mathbb{K}_u \mathbf{z}$ is exponentially stable (with decay rate governed by the shift parameter ω). We refer to Airiau et al. (2017) for the details on the initial condition required. Finally, the same linear feedback law $\mathbb{K}_u$ is used in the nonlinear system (14) (stabilizability can be proved using fixed point argument). Note that only the state variables $\mathbf{z}$ appear in the definition of the feedback input control, after the elimination of the fluid domain variables, in particular the multipliers $\boldsymbol{\eta}$ have no effect. Once the full state controller is known, we point out that the same gain matrix can be computed also for the system (34), where the fluid domain variables have not been eliminated. We recall the definition of the mass matrix in (20) and we define the matrix made by columns of the unstable adjoint eigenvectors with the fluid domain variables as:

$$\boldsymbol{\Xi}_{uns} = \begin{bmatrix} \boldsymbol{\Xi_u} \\ \boldsymbol{\Xi_{\eta,u}} \\ \boldsymbol{\Xi_{q_e,u}} \end{bmatrix}. \tag{38}$$

Finally, we can compute the same input controller as:

$$\mathbf{u}_{ctrl} = -\mathbb{B}_u^T \mathbb{P}_{\omega,u} \boldsymbol{\Xi}^T_{\boldsymbol{uns}} M \begin{bmatrix} \mathbf{z} \\ \boldsymbol{\eta} \\ \boldsymbol{q_e} \end{bmatrix}. \tag{39}$$

3.2.3. Generalized ARE

A generalized ARE version of the approach used to find $\mathbb{P}_{\omega,u}$ has been provided in Airiau et al. (2017). The shift matrix $\omega \boldsymbol{I}_{\mathbb{R}^{d_u}}$ in (36) can be modified and it is possible to use a shift Δ_u of the form $\Delta_u = \text{diag}((\omega_j \boldsymbol{I}_{\mathbb{R}^{m_j}})_{j\in J_u})$ and a control weight matrix $\boldsymbol{Q} = \text{diag}((Q_j)_{j\in J_u})$ such that $Q_j = Q_j^T \geq 0$. The term m_j denotes the dimension of the generalized eigenspace associated to the eigenvalue λ_j. The pair $(\Lambda_u + \Delta_u, \mathbb{B}_u)$ is stabilizable providing either $-\omega_j < \Re(\lambda_j)$ or $Q_j > 0$.

3.2.4. Degree of stabilizability (DoS): Choice of the unstable spectrum and actuator placement

In order to design an efficient controller, we can look at the stabilizability properties of the LTI system we are aiming to control. We recall the definition of the stabilizability Gramian $\boldsymbol{G}_{\omega,u}$ of the pair $(-\Lambda_u - \omega \boldsymbol{I}_{\mathbb{R}^{d_u}}, \mathbb{B}_u)$:

$$\boldsymbol{G}_{\omega,u} = \int_0^\infty e^{-t(\Lambda_u + \omega \boldsymbol{I}_{\mathbb{R}^{d_u}})} \mathbb{B}_u \mathbb{B}_u^T e^{-t(\Lambda_u^T + \omega \boldsymbol{I}_{\mathbb{R}^{d_u}})} dt. \tag{40}$$

In linear system control theory, the Gramian gives a criterion about the possibility to reach a final, desired state in a finite amount of time starting from an initial state. Moreover, it provides the minimum amount of control input energy one has to spend to perform this operation (Chen, 1995). Hence, as suggested in Airiau et al. (2017), we can look at the smallest eigenvalue of $\boldsymbol{G}_{\omega,u}$ to define a criterion on the degree of stabilizability (hereafter abbreviated as DoS) of the LTI system. In the case of a null weighting matrix Q, the Gramian is exactly the inverse of the solution of the Riccati equation, $\boldsymbol{G}_{\omega,u} = (\mathbb{P}_{\omega,u})^{-1}$. Hence, we can avoid building the stabilizability Gramian analyzing directly the spectrum of $\mathbb{P}_{\omega,u}$. The largest eigenvalue of the matrix $\mathbb{P}_{\omega,u}$ solution of the ARE of small dimension is a good indicator of the stabilizability of the system defined by $(\Lambda_u + \omega \boldsymbol{I}_{\mathbb{R}^{d_u}}, \mathbb{B}_u)$. We can define the DoS, denoted as d, of the pair $(\Lambda_u + \omega \boldsymbol{I}_{\mathbb{R}^{d_u}}, \mathbb{B}_u)$ as:

$$d = \max(\text{spect}(\mathbb{P}_{\omega,u}))^{-1}. \tag{41}$$

Since the largest eigenvalue of $\mathbb{P}_{\omega,u}$ depends on the biorthogonal basis of $\mathbb{Z}_u$, we prefer to use a criterion independent of the basis (see Airiau et al. (2017)). The largest eigenvalue of $\mathbb{P}_{\omega,u}$ is approximated by $\max(\text{spect}(\mathbb{S}_{\omega,u}))^{-1}$, with $\mathbb{S}_{\omega,u}$ defined as:

$$\mathbb{S}_{\omega,u} = \mathbb{W}_u \mathbb{P}_{\omega,u} \mathbb{W}_u \quad \text{with} \quad \mathbb{W}_u = (\boldsymbol{\Xi}_u^T \tilde{\boldsymbol{M}}_{\mathbf{zz}} \boldsymbol{\Xi}_u)^{1/2}. \tag{42}$$

This strategy can be also performed for J_u reduced to its minimum number of elements. This approach allows one to consider each eigenvalue λ_j separately to define the associated DoS denoted d_j. We used such information for two design choices. First, we used it to choose the patch location by comparing the stabilizability properties of the system as a function of the longitudinal position of the patches. Second, we used this information to choose the eigenvalues that should be kept in the ROM. Indeed, controlling stable eigenvalues to increase their damping could require an excessive control effort leading to overcome of saturation limits. This can be avoided by verifying that the associated dynamics is sufficiently easy to control with respect to the others, not requiring an excessive control effort.

4. Numerical results

4.1. Numerical setup and steady-state configuration

The problem (10) considered is the cylinder with a rear, flexible splitter plate in a channel. The geometry considered is similar to Turek's benchmark test case (Turek and Hron, 2006), where a slightly non-symmetrical configuration is obtained by placing the cylinder shifted from the channel symmetry plane. Here, a longer channel, with a computational domain of length $L_d = 100$, is considered to reduce the sensitivity of the spectrum to the channel length. The distance of the inlet surface Γ_{inlet} from the cylinder centre is 35 where a parabolic velocity profile $\boldsymbol{u}_{in} = 0.357(2 + y)(2.1 - y)$ is imposed. The distance of the outlet surface Γ_{outlet} from the cylinder centre is 65. On the lateral walls and on the surface of the cylinder (Γ_{wall} in (10)), we impose a no-slip condition. Taking the diameter of the cylinder as the reference length, the dimensionless length of the splitter plate is $L = 3.5$ (see Fig. 6) while the dimensionless thickness of the beam is $t_b = 0.05$. The cylinder is centred at $C = (0, 0)$. Such parameters correspond to the following dimensional values for the problem: a cylinder diameter of $\hat{D} = 0.050m$ immersed in oil with density $\hat{\rho}_f = 880Kg/m^3$ and dynamic viscosity of $\hat{\mu}_f = 287 \times 10^{-3} Pa/s$. The average inlet velocity is $\hat{U}_\infty = 1.3m/s$. For the structure, the mass ratio is $m^* = 3.5$ and the dimensional Young's modulus is $\hat{E} = 30GPa$. Such parameters correspond to a Reynolds number $Re = 200$ and a dimensionless Young's modulus of $E = 20170$. The Poisson ratio is $\nu = 0.4$. A discussion on the role of the Reynolds number and Young's modulus is reported in Appendix D. The actuators are selected among those available, see Smart Material website (n.d.). In particular, the model with an active length of $\hat{L}_p = 25\,mm$ is chosen. The thickness of the patch is $\hat{t}_p = 300\mu m$, equal for all patches. In dimensionless form, these values correspond to a patch length of $L_p = 0.5$ and $t_p = 0.006$. The piezoelectric patches have an average free-strain per volt of $\hat{\alpha} = 0.75ppm/V$ and an applicable voltage range of $[-500,\ 1500]\,V$. However, we limit our applied voltage in the range $\pm\hat{V}_{max}$, with $\hat{V}_{max} = 500\,V$. The dimensionless piezoelectric coefficient is $\alpha = 375 \times 10^{-6}$. The equations are discretized using finite elements on an adapted triangular fluid grid with 40,950 vertices and structural grid with 2255 vertices. The grid adaptation is performed thanks to the BAMG software available in *FreeFem++* (Hecht, 2012), using the *steady state* velocity field to compute the metric. We discretize the velocities and displacements by $\mathbb{P}_2$ elements and all the other quantities by $\mathbb{P}_1$ elements. The numerical discretization is performed exploiting the open-source library *GetFEM* (Renard et al., 2020). The steady state is computed dropping the time derivative terms from the nonlinear system (14) and employing Newton iterations. To warrant its convergence, a continuation of the solution has been performed to reach the equilibrium point for such parameters, starting from a rigid configuration and moving towards

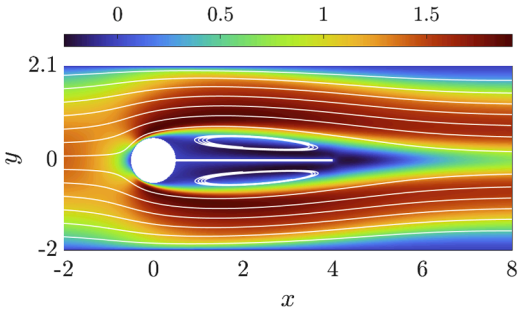

Fig. 3. Steady state ($Re = 200,\ E = 20170$). The colorbar shows the horizontal velocity field u and the streamlines are depicted in white.. (For interpretation of the references to colour in this figure legend, the reader is referred to the web version of this article.).

$Re = 200$. Then, another continuation increasing the plate flexibility has been performed to reach the desired dimensionless Young's modulus. The steady state presents a baseflow with a large separation region behind the cylinder that closes itself behind the splitter plate. The base flow is reported in Fig. 3, where the dimensionless horizontal velocity field is presented.

The steady displacement of the plate is reported in Fig. 4, where the dimensionless vertical displacement s_y of the beam mid-line is shown.

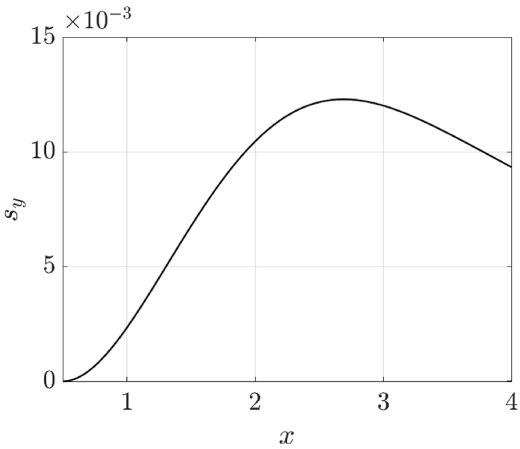

Fig. 4. Steady state ($Re = 200,\ E = 20170$). Vertical displacement s_y of the mid-line plate along its longitudinal direction.

The deformation at the equilibrium presents a slight asymmetry, and the splitter plate is slightly bent upward. The region near the free-end also presents an inverse, downward bending. However, the displacement is still quite small with respect to the reference length and reaches a maximum value around 1.2 % times the cylinder diameter. The time dependent equations have been discretized in time by a second-order Crank-Nicolson scheme and run on the same grid used for the steady problem with a constant time step $\Delta t = 0.05$. A convergence study about the spatial and temporal discretization is available in Appendix A.

4.2. No control spectrum

In this paper, we consider a two-dimensional configuration and adopt a matrix-forming approach (Loiseau et al., 2019), explicitly assembling the monolithic linearized FSI system. The spectrum is computed using the ARPACK library (Lehoucq et al., 1998). For three-dimensional problems, however, this approach becomes impractical. While the modelling framework and theoretical justification remain valid, allowing the system to be written in controllable form via a suitable projector, the main limitation lies in the numerical computation of spectra for extremely large systems. To overcome this problem, matrix-free methods (Loiseau et al., 2019), based on efficient time-stepper direct and adjoint solvers, could be employed, as in Bagheri et al. (2009), to investigate the stability and control of high-dimensional systems.

For the parameters under investigation, the spectrum of the FSI linearized problem (17), shown in Fig. 5a has three unstable, complex-conjugate modes λ_j, for $j = 1, \cdots, 6$. Moreover, in the stable part with the lowest damping ratio, we find other modes λ_j, for $j = 7, \cdots, 13$, that can be collected into a set of three real modes and two complex conjugate pairs. The other stable modes belong to a continuous branch that is well damped. For this configuration and set of parameters, at least the three unstable dynamics must be controlled. The most unstable mode, at high frequency, corresponds to a pair of complex conjugate eigenvalues $\lambda_{1,2} = 0.351 \pm 2.33\, i$ (black filled dots in Fig. 5a). This mode excites mainly the third structural mode, as can be seen in Fig. 5b from the plot of the beam

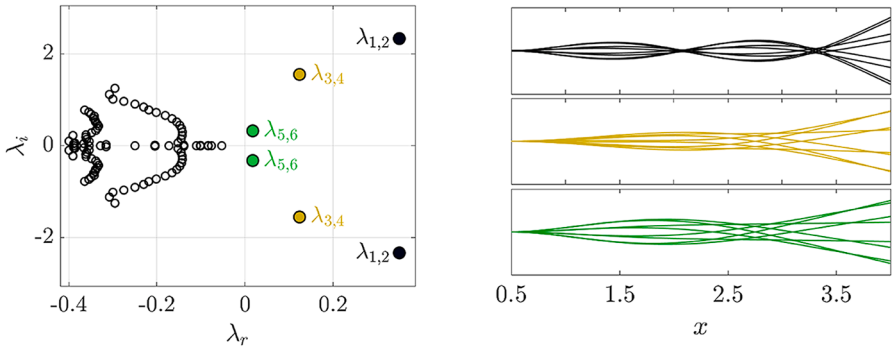

(a) Significant set of eigenvalues that form the spectrum of the FSI system. The unstable modes are highlighted: $\lambda_{1,2}$ (black filled dots), $\lambda_{3,4}$ (yellow filled dots), $\lambda_{5,6}$ (green filled dots).

(b) Representation of 8 different phases of the structural deformation for the modes $\lambda_{1,2}$ (black), $\lambda_{3,4}$ (yellow) and $\lambda_{5,6}$ (green) along the mid-line plate longitudinal direction.

Fig. 5. No-control spectrum (17) defined by the set of eigenvalues $\lambda = \lambda_r \pm i\lambda_i$, where λ_r is the real part of each eigenvalue and λ_i is its imaginary part.

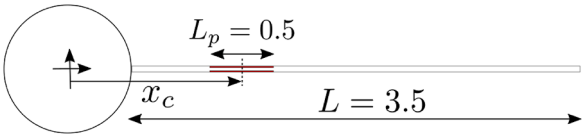

Fig. 6. Configuration used to scan the beam with one pair of actuators (in red). (For interpretation of the references to colour in this figure legend, the reader is referred to the web version of this article.).

deformation for some oscillation phases. The second unstable mode is at intermediate frequencies, with a couple of complex conjugate eigenvalues $\lambda_{3,4} = 0.124 \pm 1.55\,i$ (yellow filled dots in Fig. 5a). This mode has a smaller amplification rate with respect to the first one. The third unstable mode has the lowest frequency, $\lambda_{5,6} = 0.0178 \pm 0.323\,i$ (green filled dots in Fig. 5a) and it is the least unstable one. The plate deformation due to this mode is reported in Fig. 5b, showing that the deformation is close to that of the second bending mode of the plate. For modes $\lambda_{3,4}$ and $\lambda_{5,6}$, the coupling of the structure with the fluid leads to a structural vibration mode which is very different from the natural bending mode of the beam. Indeed, its deformation resembles more a travelling wave deformation than a pure bending oscillation.

4.3. Stabilizability analysis and ROM definition

The solution of the Algebraic Riccati Equation (ARE) allows us to build the optimal feedback controller for the LTI system obtained from the linearization around the steady state (17). However, the number of actuators and their distribution on the beam are design choices that influence a lot the quality of the controller. Indeed, for different flow and structural parameters, we can look at several instability mechanisms that trigger different structural modes. Each one can be controlled in an efficient way that is not the same for all. If we know what structural mode is excited from the unstable mode, we can decide the placement and number of actuators necessary to control it in a precise and efficient way. For example, if the first bending mode is mainly excited by a FSI coupling, the actuator must be placed in a region where the first bending mode is more receptive. However, due to the non-normality of the fluid-structure operator, this location is not easily determined. In order to have a criterion to select the best position where the actuators have to be placed, we used the degree of stabilizability (DoS) criterion based on the associated Gramian in (41). We performed a preliminary analysis with a single pair of actuators, one on the top side of the flexible plate and the other on the bottom side, and we systematically changed the position of them, testing 200 different positions uniformly distributed. We denote the dimensionless coordinate of the centre of the patch with x_c, measured in the undeformed configuration. An example that clarifies the configuration is shown in Fig. 6. We changed $x_c \in [0.75, 3.75]$ to scan all the beam length. The scan of the beam changing the position of the actuators is very quick due to the fact that the ROM is unchanged for different positions of the MFC. This is because the MFC patch and the non-actuated region have the same structural parameters. To update the location of the MFC in the ROM, the only term that has to be recomputed is the control matrix $\mathbb{B}_u$ in (35).

At each position, we computed the DoS d_j, for each $j \in J_u$ in (41) and we identified the peaks of stabilizability to choose the number and the location of the actuators. In this analysis, we solved the generalized ARE with a parameter $\omega \boldsymbol{I}_{\mathbb{R}^{m_j}} = 0.3\boldsymbol{I}_{\mathbb{R}^{m_j}}$.

Moreover, we conduct a comparison with the stability analysis results, looking at both the direct and adjoint modes in the structure. The differences between the direct and adjoint eigenvectors are due to the non-normality of the fluid operators that can produce a very large difference between them, while the elasticity operator is self-adjoint. We reported the results for the DoS for each unstable mode in Fig. 7a–c, where each dot represents the position of the MFC patch tested. The results are compared with the norm of the direct-

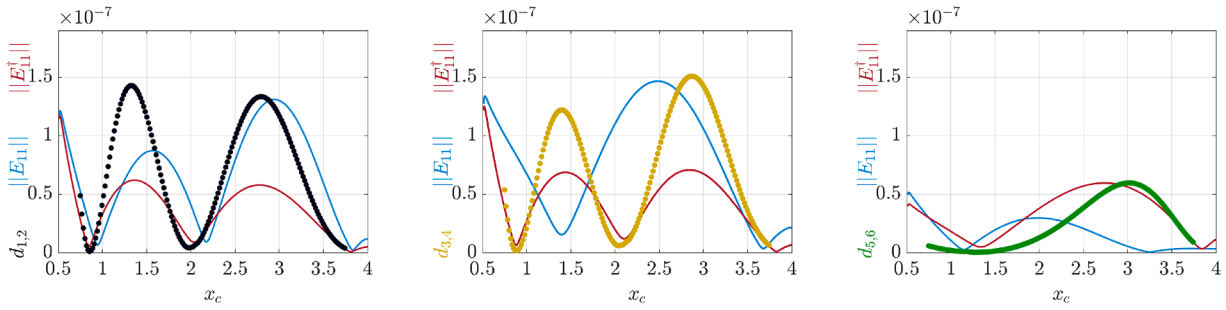

Fig. 7. Comparison between the degree of stabilizability and the norm of the direct E_{11} (blue line) and adjoint $E_{11}^{\dagger}$ (red line) mode axial strain for the mode $\lambda_{1,2}$ (a), $\lambda_{3,4}$ (b), $\lambda_{5,6}$ (c). Degree of stabilizability $d_{1,2}$ (black dots), $d_{3,4}$ (yellow dots) and $d_{5,6}$ (green dots). (For interpretation of the references to colour in this figure legend, the reader is referred to the web version of this article.).

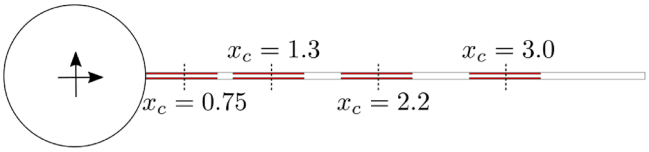

Fig. 8. MFC placement based on the degree of stabilizability (DoS) criterion.

Table 1
Degree of stabilizability (DoS) for several patch numbers and location ($\omega = 0.3$).

$10^7 d_j$	$\lambda_{1,2}$	$\lambda_{3,4}$	$\lambda_{5,6}$
1 couples	0.40	0.46	0.06
2 couples	1.88	1.71	0.06
4 couples (uniform distribution)	2.68	3.01	0.99
4 couples (DoS based distribution)	3.37	3.40	0.95

and adjoint-mode axial strain E_{11}, extracted from the Lagrangian stress tensor **E**. We observe that for all unstable modes, the peaks of the DoS coincide with the peaks of the adjoint-mode axial strain. Moreover, we note that if we look at the direct modes only, the predictions can be very misleading. This is especially the case for the modes $\lambda_{3,4}$ and $\lambda_{5,6}$ where the non-normality effects are evident. Indeed, the structural deformation is a travelling wave and not a purely stationary, oscillatory bending mode (see Fig. 5b) and the peaks of the DoS appear where a minimum axial strain of the direct mode is observed (see Fig. 7b and c). We compare all the results of the stabilizability analysis for the unstable modes and we decide to use 4 couples of actuators centred in $x_c = [0.75, 1.3, 2.2, 3.0]$. The final placement is shown in Fig. 8.

This design choice is then compared with other locations in terms of stabilizability. Therefore, we computed the degree of stabilizability (DoS) for the three unstable modes with a different number and location of the patches. We tested four different configurations. The first one is made by a couple of patches, placed on the clamped root of the beam. The second configuration uses the two MFC pairs closest to the cylinder in Fig. 8. In this configuration $x_c = [0.75,\ 1.3]$. The third choice corresponds to use four patches uniformly distributed all over the beam: $x_c = [0.75,\ 1.625,\ 2.5,\ 3.375]$. The last one uses four patches placed in the positions identified by the scan of the beam with one pair of MFC (see Fig. 8) and based on the DoS criterion. We solved the generalized ARE with the additional term $\omega \boldsymbol{I}_{\mathbb{R}^{m_j}} = 0.3\boldsymbol{I}_{\mathbb{R}^{m_j}}$. The results are shown in Table 1 and confirm that the selected placement performs well with respect to the other cases.

In fact, a single patch has a very low degree of stabilizability with respect to four patches. Two couples of patches show a good stabilizability for the modes $\lambda_{1,2}$ and $\lambda_{3,4}$, due to the fact that their placement matches the first two peaks of stabilizability at $x_c \approx 0.75$ and $x_c \approx 1.5$. However, they lead to very poor stabilizability for the other mode because they do not match the peak in $x_c \approx 3.0$. Four uniformly distributed patches increase the stabilizability of every mode. However, it is still outperformed by the placement based on the DoS. We also verified the stabilizability of the modes associated with the stable eigenvalues closest to the imaginary axis. In particular, we looked at the DoS of the modes with eigenvalues $\lambda_7 = -0.053$, $\lambda_8 = -0.076$, $\lambda_{9,10} = -0.084 \pm 0.0019\,i$, $\lambda_{11,12} = -0.10 \pm 0.0058\,i$ and $\lambda_{13} = -0.11$. We report the results in Table 2 with the placement based on the DoS of the MFC actuators.

We notice that their stabilizability is very poor, so we decided not to include them in the controlled subspace $\mathbb{Z}_u$. Therefore, the Reduced Order Model is built taking only the unstable dynamics into account.

Table 2
Degree of stabilizability ($10^7\, d_j$) of other modes with the location based on the DoS ($\omega = 0.3$).

Eig.	λ_7	λ_8	$\lambda_{9,10}$	$\lambda_{11,12}$	λ_{13}
$10^7 d_j$	3.44×10^{-2}	2.32×10^{-2}	6×10^{-8}	2.8×10^{-5}	1.2×10^{-5}

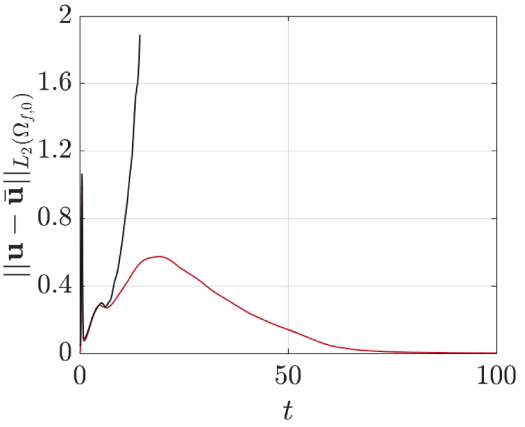

Fig. 9. Velocity field error in $L_2(\Omega_{f,0})$ norm for no control (black) and controller designed with $\omega = 0$ (red). (For interpretation of the references to colour in this figure legend, the reader is referred to the web version of this article.).

4.4. Closed-loop system: Stabilization, control effort and error evaluation

Once the ROM is built over the selected dynamics, a small dimension plant is obtained and the classical methods of optimal control can be applied. The closed-loop ROM is then built defining a feedback control input of the form $\mathbf{u}_{ctrl} = -\mathbb{B}_u^T \mathbb{P}_{\omega,u} \boldsymbol{\zeta}_{\boldsymbol{u}}$ in (35). To control all the dynamics, four couples of patches are employed as shown in Fig. 8. Two different strategies are adopted to stabilize the closed-loop system, based on the selected design parameter ω. A first option is to choose $\omega = 0$. In this way, the unstable spectrum will be reflected with respect to the imaginary axis. The stabilization of the plant is tested with a time marching simulation. The steady state solution is used as initial condition at time $t_0 = 0$ and a disturbance $u_d(y,t) = \beta h(y) g(t)$ is added to the inlet boundary condition to perturb the equilibrium ($\boldsymbol{u} = \boldsymbol{u}_{in} + (u_d(y,t), 0)^T$ on Γ_{inlet}), with $g(t) = e^{-30(t-0.5)^2}$ and $h(y) = 0.357(2+y)(2.1-y)$. The size of the disturbance is set by the coefficient β. In the present case, a 5 % increase of the inlet velocity with respect to the *baseflow* was enforced. The control effort is evaluated looking at the control input vector $\mathbf{u}_{ctrl}$ that collects the dimensionless voltage ΔV_i, for each i–th patch.

At the same time, the distance of the current solution from the target steady solution is computed in the $L_2(\Omega_{f,0})$–norm of the velocity field. We start with the case without any control action. For this system (10), the open-loop unstable spectrum suggests an unstable equilibrium that, once perturbed, moves away from the *steady state* considered. The time marching solution confirms such a trend as shown in Fig. 9, with a distance with respect to the *steady state* solution that increases in time.

The uncontrolled simulation reaches a maximum time at which the ALE approach fails and the run stops. This is a classical limitation of the ALE approach in case of large deformations that can lead to the collapse or the inversion of the triangular elements of the fluid domain discretization (Shamanskiy and Simeon, 2021). We then introduce the controller designed with $\omega = 0$. In this case, by virtue of the feedback controller, the three complex conjugate pairs of unstable modes $\lambda_{1,2}$, $\lambda_{3,4}$ and $\lambda_{5,6}$ in Fig. 5a are stabilized. The eigenvalues of the controlled ROM (35) and (36) are $\lambda_{1,2_{CL}} = -0.351 \pm 2.33\, i$, $\lambda_{3,4_{CL}} = -0.125 \pm 1.55\, i$ and $\lambda_{5,6_{CL}} = -0.0169 \pm 0.323\, i$, where the subscript $_{CL}$ denotes the closed-loop dynamics to distinguish it from the uncontrolled case. In the time marching simulation, we can see the initial perturbation of the system and how the plant reacts. The error is shown in Fig. 9 and has a spike due to the initial perturbation. Once the inlet perturbation has disappeared, the perturbed system starts to move away from the steady solution. However, after an initial transient where the error reaches its maximum value, the controller stabilizes the plant. The control inputs for each patch are shown in Fig. 10.

A large voltage input is applied by the controller in the first time steps to control the perturbation, then the control inputs decrease with time. These results confirm that no patch reaches the maximum applicable voltage and the system can damp the perturbation and stabilize the system. A visualisation of the stabilizability effect of this controller is reported in Fig. 11b where a set of four snapshots from the time marching simulations is extracted, for both the uncontrolled case and the controlled case in four different time steps. The horizontal velocity field for the uncontrolled case in Fig. 11a clearly shows the growth of the perturbation in the channel and the initial oscillations of the flexible plate due to the surrounding flow. On the contrary, on the controlled case panels in Fig. 11 it is noticeable that the controller avoids the growth of the flow disturbances and prevents the plate to start vibrating.

The time marching simulation of the controlled case with $\omega = 0$ is also compared to the controlled case with the same parameter ω but with a different distribution of the patches along the plate. In this way, the improvements achievable by the patch distribution

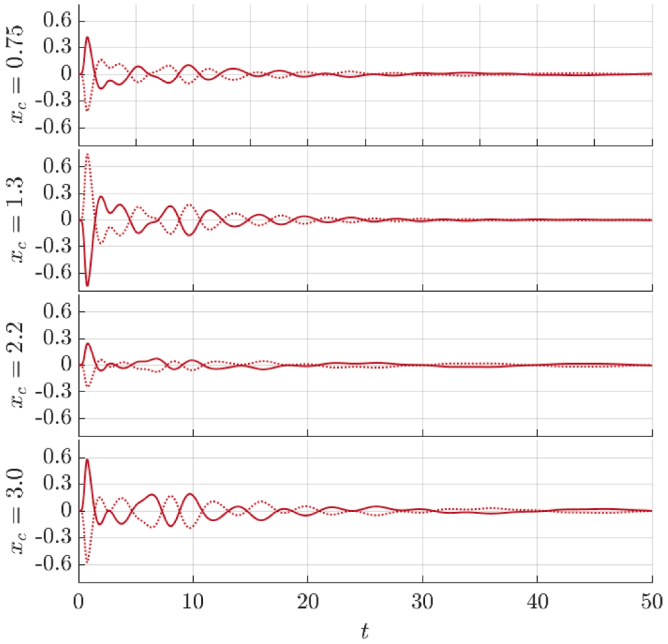

Fig. 10. Control inputs for $\omega = 0$. Continuous lines are used for the patches on the top side, dotted lines for the patches on lower side of the beam. The couples of patches are located in $x_c = [0.75,\ 1.3,\ 2.2,\ 3.0]$.

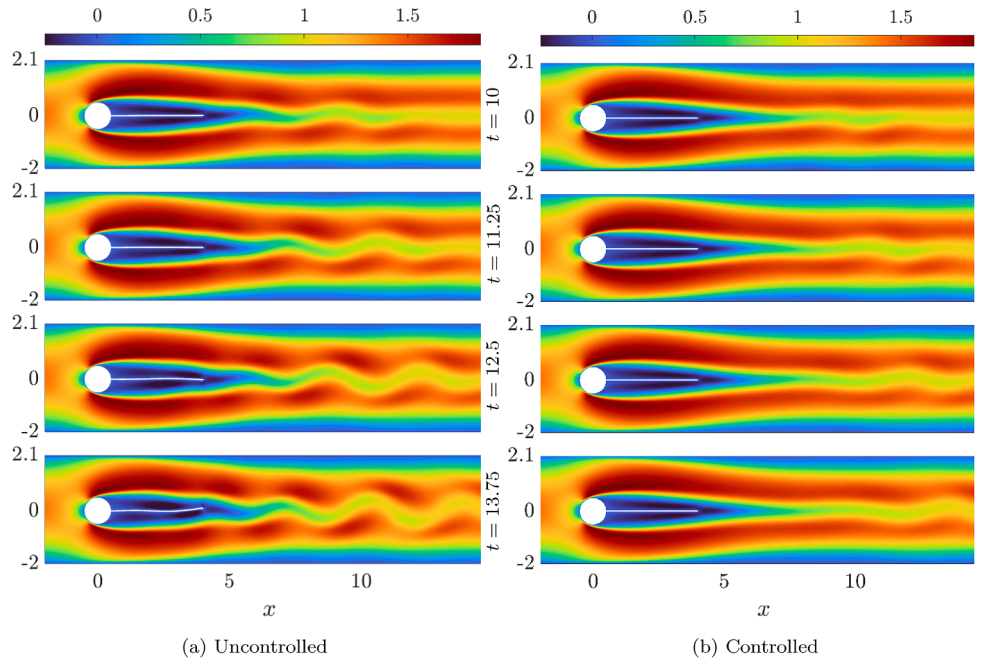

Fig. 11. Horizontal component of the velocity field. Time marching simulations for the uncontrolled case (a) and controlled case (b) with the control inputs for $\omega = 0$.

based on the DoS along the plate is verified by means of a comparison with another placement expected to be worse from the stabilizability analysis. We design a controller with $\omega = 0$ and we consider four patches uniformly distributed along the plate, with $x_c = [0.75,\ 1.625,\ 2.5,\ 3.375]$. We compare in Fig. 12 the error in time of the velocity field with respect to the steady state and the energy input $\mathbf{u}_{ctrl}^T\,\mathbf{u}_{ctrl}$ in the two cases under discussion. We can highlight that the error on the velocity field is marginally different, due to the fact that the same closed loop system is retrieved in both cases. However, the stabilizability with the uniform patch distribution requires a larger control input energy during the whole simulation, confirming the results obtained by the stabilizability analysis previously discussed.

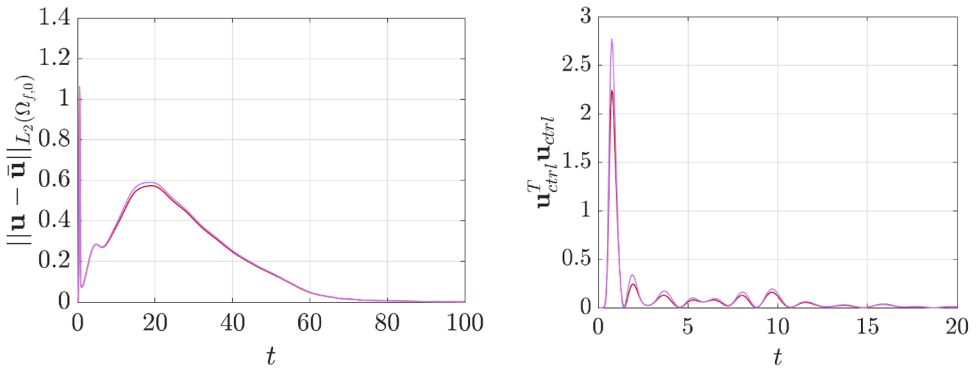

Fig. 12. Velocity field error (left) in $L_2(\Omega_{f,0})$ norm for placement based on the DoS of the 4 couples of the actuators (red) and 4 couples of actuators uniformly distributed (violet) with a closed-loop controller $\omega = 0$. Input energy $\mathbf{u}_{ctrl}^T\mathbf{u}_{ctrl}$ for $\omega = 0$ (right) for the placement distribution based on the DoS (red) and uniform distribution (violet). (For interpretation of the references to colour in this figure legend, the reader is referred to the web version of this article.).

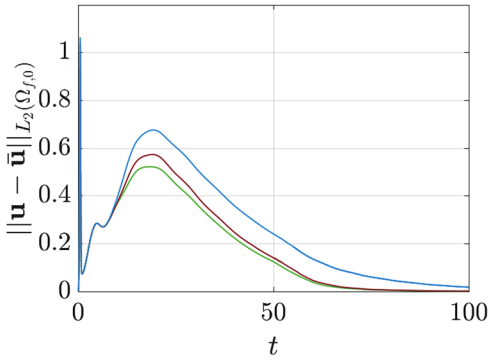

Fig. 13. Velocity field error in norm $L_2(\Omega_{f,0})$ for the controllers with $\omega = 0$ (red), $\omega = 0.2$ (green) and $\Delta_u = \mathrm{diag}(\omega_j \mathrm{I}_{\mathbb{R}^2})$ (blue) in case of a perturbation amplitude $\beta = 5\,\%$. . (For interpretation of the references to colour in this figure legend, the reader is referred to the web version of this article.).

4.4.1. *Effect of ω*

The choice of different ω influences the control effort and the time to damp the oscillations and to stabilize the system towards the steady state. A deeper investigation of the effect of ω in the controller design is performed using the placement of the actuators in Fig. 8. Firstly, we designed a controller selecting a parameter $\omega = 0.2$. In this case, by virtue of the feedback controller, the three complex conjugate pairs of unstable modes $\lambda_{1,2}$, $\lambda_{3,4}$ and $\lambda_{5,6}$ in Fig. 5a are stabilized. The eigenvalues of the controlled ROM (35) and (36) are $\lambda_{1,2_{CL}} = -0.751 \pm 2.33\,i$, $\lambda_{3,4_{CL}} = -0.524 \pm 1.55\,i$ and $\lambda_{5,6_{CL}} = -0.418 \pm 0.323\,i$ and they are obtained mirroring the unstable spectrum with respect to the axis defined by $\lambda_r = -\omega = -0.2$. Another design is subsequently proposed. In this case, the parameter ω is tuned to have the stabilized eigenvalues of the closed-loop ROM (35) and (36) with similar real part. We use the general version of the ARE (see Section 3.2.3) with a shift Δ_u of the form $\Delta_u = \mathrm{diag}((\omega_j \mathrm{I}_{\mathbb{R}^{m_j}})_{j\in J_u})$, and the unstable subspace is associated to three unstable complex conjugate pairs of eigenvalues. For this reason, as previously stated, the unstable subspace is defined by the modes λ_j, with $j \in \{1, 3, 5\}$ and $m_j = 2$ due to the fact that we are dealing with complex conjugate pairs. The idea is to choose three different ω_j, moving the unstable eigenvalues so as to approximately obtain a desired real part for all of them in the closed-loop system. The aim is twofold: the first design of the controller stabilizes too much the most unstable dynamics, with a real part for the closed loop modes largely smaller than that of the other stable modes. Moreover, we would like to reduce the control effort to avoid exceeding the maximum allowed voltage, by avoiding an excessive stabilization. In this case, we pick $\omega_{1,2} = -0.150$, $\omega_{3,4} = -0.0371$ and $\omega_{5,6} = 0.0161$ aiming at approximating the desired real part of the eigenvalues around -0.05 for all the closed-loop dynamics. The real part of the closed-loop modes can be strategically chosen to be close to that of the least stable modes of the $\mathbb{Z}_s$ subspace. For each eigenvalue, we respect the condition $\omega_j > -\Re(\lambda_j)$. With this choice, the eigenvalues of the controlled ROM (35) and (36) are $\lambda_{1,2_{CL}} = -0.0379 \pm 2.33\,i$, $\lambda_{3,4_{CL}} = -0.0616 \pm 1.55\,i$ and $\lambda_{5,6_{CL}} = -0.0505 \pm 0.323\,i$. Notice that, while the real parts of these eigenvalues are different, their orders of magnitude are the same. These two new additional closed loop controllers are tested with a time marching scheme and the same inlet perturbation used in the previous case is considered. The results for the error with respect to the steady-state solution are reported in Fig. 13 while the control inputs for the patches with the largest input are reported in Fig. 14.

For the controller with $\omega = 0.2$, the growth of the perturbation reaches a maximum value when $t \approx 20$ and its peak is lower with respect to the case of $\omega = 0$ (see Fig. 13). Moreover, the error with respect to the steady state is always lower with respect to the first controller ($\omega = 0$), which means that the controller with $\omega = 0.2$ is faster with respect to the controller with $\omega = 0$ as expected,

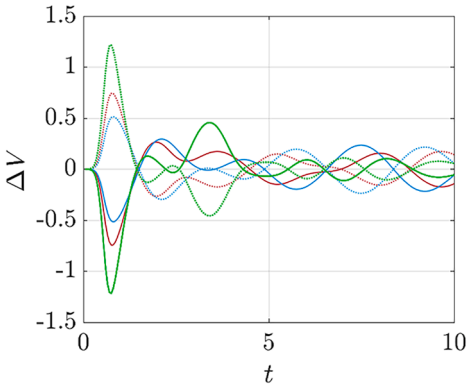

Fig. 14. Control inputs for the patches centred in $x_c = 1.3$ for $\omega = 0$ (red), $\omega = 0.2$ (green) and $\Delta_u = \mathrm{diag}(\omega_j \mathrm{I}_{\mathbb{R}^2})$ (blue). Continuous line: patch placed on the top side; dotted line: patch placed on the bottom side.. (For interpretation of the references to colour in this figure legend, the reader is referred to the web version of this article.).

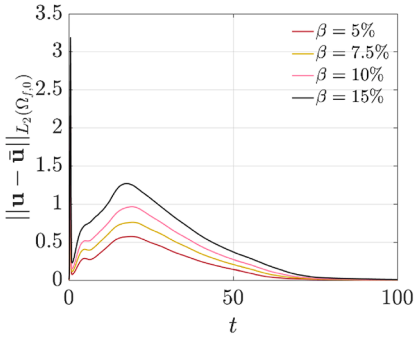

(a) Velocity field error in norm $L_2(\Omega_{f,0})$.

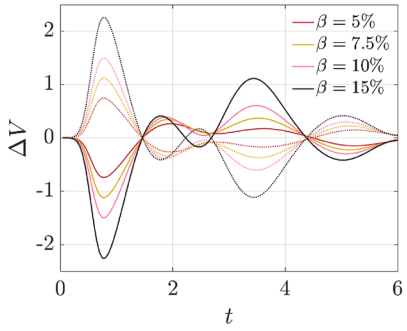

(b) Control inputs on the patches centred in $x_c = 1.3$. Continuous line for patch on the top side and dotted line for patch on the bottom side.

Fig. 15. Effect of the perturbation amplitude $\beta = [5\,\%, 7.5\,\%, 10\,\%, 15\,\%]$ on the controller designed with $\omega = 0$.

because the unstable modes are more stabilised by the second controller. In fact, the $L_2(\Omega_{f,0})$ error norm reaches the value 0.1 at $t \approx 55$ for the first controller, while the same value is reached at $t \approx 53$ for this second, new controller ($\omega = 0.2$). This increase in performance comes at a price, because this faster stabilisation is achieved by a larger control input with respect to the first controller, as clarified in Fig. 14 where we focus our attention only on the mainly excited patch that is centred in $x_c = 1.3$. We note that the controller with $\omega = 0.2$ reaches a maximum applied voltage $\Delta V_{3,4} \approx 1.2$ that is far larger than the control input of the first controller $\Delta V_{3,4} \approx 0.75$. Moreover, the input value required by the second controller saturates the constraints of the actuator for the same perturbation amplitude considered. We discuss now the third controller designed by the generalized shift $\Delta_u = \mathrm{diag}((\omega_j \mathrm{I}_{\mathbb{R}^{m_j}})_{j \in J_u})$. In this case, after the perturbation and the growth of the error until $t = 20$, the stabilization is significantly slower with respect to the first ($\omega = 0$) and second ($\omega = 0.2$) controller and the error reaches a value of 0.1 when $t \approx 65$. However, this choice of the control parameters reduces the control input needed to stabilize the plant. In fact, comparing the control inputs for the three controllers in Fig. 14, we can observe significant differences.

The maximum control input is $\Delta V_{3,4} \approx 0.75$ for the first controller and $\Delta V_{3,4} \approx 0.5$ for the new, third controller, resulting in a reduction in the required control input of approximately 30 %. This is due to the fact that we are modifying the closed-loop spectrum, in particular reducing the damping for the two most unstable open-loop dynamics $\lambda_{1,2_{CL}}$ and $\lambda_{3,4_{CL}}$.

4.4.2. Effect of perturbation amplitude (parameter β)

In this section, we discuss the effect of the size of the perturbation amplitude by changing the value of β. The scope is twofold. Firstly, our objective is to define the largest inlet perturbation amplitude for which the saturation constraints of the actuators are not overcome. Moreover, our aim is to test the optimal controller, designed in a linear framework, in the nonlinear system with a large perturbation. We perform a time-marching simulation of the controller with $\omega = 0$ and the one designed by $\Delta_u = \mathrm{diag}(\omega_j \mathrm{I}_{\mathbb{R}^2})$. We use the same fluid and dimensionless structure parameters and the same shape of the inlet perturbation. The controller with $\omega = 0.2$ saturates the constraints of the MFC even in the $\beta = 5\,\%$ case. We change the amplitude of the perturbation in the range $\beta \in [7.5\,\%, 10\,\%, 15\,\%]$ and report in Figs. 15 and 16 the error norm with respect to the steady state solution and the input control of the most excited actuator, which is the one centred in $x_c = 1.3$. We note that both controllers, designed in the linear framework,

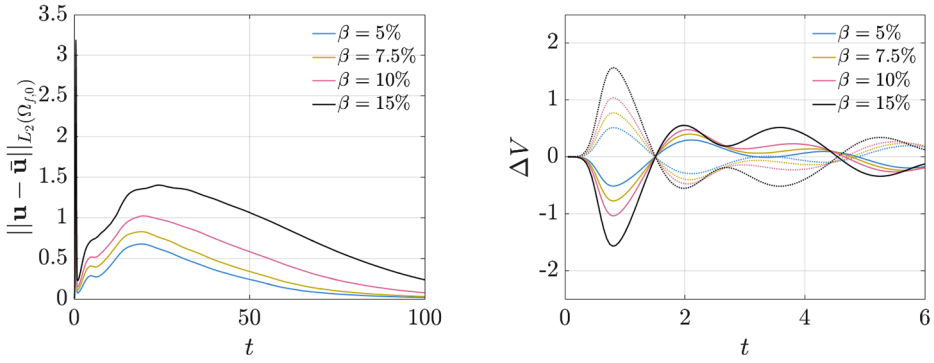

(a) Velocity field error in norm $L_2(\Omega_{f,0})$.

(b) Control inputs on the patches centred in $x_c = 1.3$. Continuous line for patch on the top side and dotted line for patch on the bottom side.

Fig. 16. Effect of the perturbation amplitude $\beta = [5\,\%, 7.5\,\%, 10\,\%, 15\,\%]$ on the controller designed with $\Delta_u = \text{diag}(\omega_j \mathrm{I}_{\mathbb{R}^2})$.

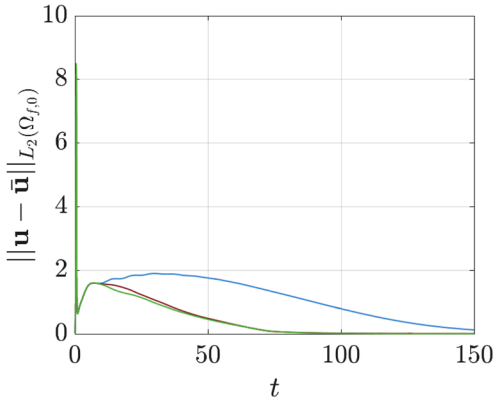

Fig. 17. Velocity field error in norm $L_2(\Omega_{f,0})$ for the controllers with $\omega = 0$ (red), $\omega = 0.2$ (green) and $\Delta_u = \text{diag}(\omega_j \mathrm{I}_{\mathbb{R}^2})$ (blue) in case of a perturbation amplitude $\beta = 40\,\%$. (For interpretation of the references to colour in this figure legend, the reader is referred to the web version of this article.).

still control the nonlinear system even in the presence of larger disturbances. If the controller designed with $\omega = 0$ overcomes the saturation limit for the case $\beta = 7.5\,\%$, the controller designed with $\Delta_u = \text{diag}(\omega_j \mathrm{I}_{\mathbb{R}^2})$ can stabilize the system without overcoming it up to $\beta = 10\,\%$.

Other tests have been performed with a larger perturbation amplitude $\beta = 40\,\%$. In this case, we are only interested to verify the stabilization ability of each controller, designed in the linear framework, in case of a large disturbance. The control inputs are not reported because every controller saturates for a smaller perturbation as already discussed. A possible improvement, to increase the saturation limits, could result from adding more patches along the thickness of the splitter plate in the same longitudinal position of the patch that saturates. For simplicity, here we maintain the same configuration investigated before and perform a time marching simulation for the three controllers designed with $\omega = 0$, $\omega = 0.2$ and $\Delta_u = \text{diag}(\omega_j \mathrm{I}_{\mathbb{R}^2})$. The velocity field error is reported in Fig. 17. We observe that every controller is still able to stabilize the unstable nonlinear system even under a perturbation amplitude $\beta = 40\,\%$.

5. Conclusion

In the present work, we propose a new control system for the FSI problem proposed by Turek (Turek and Hron, 2006). The control system is based on MFC actuators installed on the compliant splitter plate. We leverage optimal control and design the optimal regulator in a fully coupled ALE formulation that takes into account the flow equations, the structure equations with the piezoelectric patches and the equations describing the deformation of the fluid domain. To tackle this high-dimensional problem, we deduce a Reduced Order Model based on the spectral decomposition in the unstable subspace, so that the solution of the Algebraic Riccati Equation used to define the control is trivial. In the process, we also prove that we can eliminate the equations for the domain deformation introduced by the ALE formulation without affecting the controller design. We derive an original oblique projector and prove that the system obtained eliminating the multipliers and the domain deformation has the same dynamical properties as the complete system. We propose a criterion to design the placement of the actuators by computing the degree of stabilizability (DoS)

based on the associated Gramian in the Reduced Order Model and we compare the placement based on this criterion with others. We firstly show the effectiveness of the control system by direct numerical simulations of the system at a Reynolds number as high as 200, forced by a perturbation in the order of 5 % of the base-flow velocity and we verify that the placement of the actuators based on the DoS outperforms the other possible placement tested. Subsequently, we perform an investigation on the role of the controller design in the stabilization of the unstable FSI system and we discuss about the maximum perturbation amplitude each controller can stabilize. In this way, we check that the designed controllers are able to stabilize the full nonlinear system without exceeding the actuator limits.

CRediT authorship contribution statement

Simone Cruciani: Investigation; **Franco Auteri:** Investigation; **Michel Fournié:** Investigation.

Data availability

No data was used for the research described in the article.

Declaration of competing interest

The authors declare that they have no known competing financial interests or personal relationships that could have appeared to influence the work reported in this paper.

Appendix A. Spatial and temporal discretization convergence

We performed a convergence analysis to show that the numerical results presented above are not influenced by the discretization we are using. We compute the unstable spectrum for a set of three fluid meshes, labeled as M_1, M_2 and M_3 in Table A.1, keeping the same structural grid. The coarse mesh M_1 has a number of vertices of $N_p \approx 8000$, the medium mesh M_2 has $N_p \approx 20000$ and the fine mesh M_3 has a number of vertices $N_p \approx 40000$. The mesh M_3 is the one used for the numerical results in Section 4. We compute the set of the three complex conjugate eigenvalues $\lambda_{1,2}$, $\lambda_{3,4}$ and $\lambda_{5,6}$ for each mesh and we report the results in Table A.1.

Table A.1
Mesh convergence unstable spectrum. N_p number of points.

	M_1	M_2	M_3
$N_p \approx$	8000	20000	40000
$\lambda_{1,2}$	0.3461 ± 2.328	0.3508 ± 2.329	0.3510 ± 2.329
$\lambda_{3,4}$	0.1247 ± 1.554	0.1247 ± 1.550	0.1242 ± 1.550
$\lambda_{5,6}$	0.01224 ± 0.3252	0.01786 ± 0.3228	0.01775 ± 0.3227

We note the imaginary part of the unstable eigenvalues present marginal differences spanning from the coarse to fine mesh. The largest difference is in the mode $\lambda_{5,6}$ on the coarse mesh with respect to the fine one, but the relative difference is below 1 %. The growth rate of the modes $\lambda_{1,2}$ and $\lambda_{5,6}$ is slightly underestimated by the coarse spatial discretization, but the relative differences between the medium and the fine grids confirm that the results are no more grid-dependent and the grid M_3 used in the paper is fine enough to accurately predict the unstable spectrum. According to the results reported in Boffi (2010), computing up to a precision of order 10^{-2} seems to be a good compromise between precision and computation time.

We perform a convergence analysis on the time discretization used in the direct numerical simulations of the FSI system. We used the fine grid M_3 and we vary the time step Δt used in the time stepper, using a Crank–Nicolson time discretization. We simulate the controlled case with the designed controller $\omega = 0$, using the same perturbation used in the Section 4 and we integrate in time the equations with five time step values $\Delta t = [0.15, 0.1, 0.05, 0.025, 0.0125]$. We report the results about the influence of the time discretization on the velocity field error with respect to the steady state $\bar{\mathbf{u}}$ in the five time discretization adopted in Fig. A.1.

We conclude that, the time step $\Delta t = 0.05$ retained in the Section 4 is accurate enough and it is a good compromise between computational cost and accuracy for the simulations presented in this paper.

Appendix B. Definition of the oblique projector Π^T

We aim to build an oblique projector Π^T onto $\mathrm{Ker}(\tilde{\mathrm{A}}^{\mathrm{T}}_{\mathbf{z}\eta})$ parallel to $\mathrm{Im}(\tilde{\mathrm{M}}^{-1}_{\mathbf{zz}}\mathrm{A}_{\mathbf{z}\eta})$, with $\tilde{A}^T_{\mathbf{z}\eta} = A^T_{\mathbf{z}\eta} - A_{\eta q_e} A^{-1}_{q_e q_e} A_{q_e \mathbf{z}}$. We can decompose $\mathbf{z}$ as:

$$\mathbf{z} = \mathbf{z}_{\Pi^T} + \tilde{M}^{-1}_{\mathbf{zz}} A_{\mathbf{z}\eta}\boldsymbol{\eta} \tag{B.1}$$

for $\mathbf{z}_{\Pi^T} \in \mathrm{Ker}(\tilde{\mathrm{A}}^{\mathrm{T}}_{\mathbf{z}\eta})$ and $\tilde{M}^{-1}_{\mathbf{zz}} A_{\mathbf{z}\eta}\boldsymbol{\eta} \in \mathrm{Im}(\tilde{\mathrm{M}}^{-1}_{\mathbf{zz}}\mathrm{A}_{\mathbf{z}\eta})$ and state that the projected part belongs to $\mathrm{Ker}(\tilde{\mathrm{A}}^{\mathrm{T}}_{\mathbf{z}\eta})$ which allows us to write:

$$\tilde{A}^T_{\mathbf{z}\eta}\mathbf{z} = \tilde{A}^T_{\mathbf{z}\eta}\tilde{M}^{-1}_{\mathbf{zz}} A_{\mathbf{z}\eta}\boldsymbol{\eta}. \tag{B.2}$$

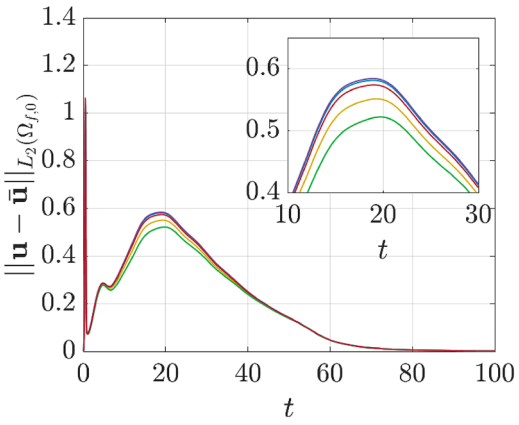

Fig. A.1. Error on the velocity field with respect to the steady solution over time computed in $L_2(\Omega_{f,0})$ norm. Convergence study with the same controller ($\omega = 0$) and five time steps Δt = [0.15 (green), 0.10 (yellow), 0.05 (red), 0.025 (blue), 0.0125 (violet)]. In the subplot: zoom on the error in the time interval $t \in [10, 30]$. (For interpretation of the references to colour in this figure legend, the reader is referred to the web version of this article.).

For the elimination to be valid, we have to prove the invertibility of the matrix $\tilde{M}_{\mathbf{zz}}$ first and we use the following notation for the matrix $A^{-1}_{q_e q_e} = \begin{bmatrix} A^{inv}_{\xi\xi} & A^{inv}_{\xi\lambda_e} \\ A^{inv}_{\lambda_e\xi} & A^{inv}_{\lambda_e\lambda_e} \end{bmatrix}$ that allows us to build explicitly $\tilde{M}_{\mathbf{zz}}$ from its definition:

$$\tilde{M}_{\mathbf{zz}} = \begin{bmatrix} M_{ss} & 0 & 0 \\ 0 & M_{u_s u_s} & 0 \\ 0 & 0 & M_{uu} \end{bmatrix} - \begin{bmatrix} 0 & 0 & 0 \\ 0 & 0 & 0 \\ M_{u\xi} A^{inv}_{\xi\lambda_e} A_{\lambda_e s} & 0 & 0 \end{bmatrix}, \tag{B.3}$$

which does not preserve the block-diagonal structure of the mass matrix $M_{\mathbf{zz}}$, due to an off-diagonal block that, in any case, does not affect its invertibility. Notice that from (B.2), the variable $\boldsymbol{\eta}$ is known from the state $\mathbf{z}$:

$$\boldsymbol{\eta} = \left[\tilde{A}^T_{\mathbf{z}\eta} \tilde{M}^{-1}_{\mathbf{zz}} A_{\mathbf{z}\eta}\right]^{-1} \tilde{A}^T_{\mathbf{z}\eta} \mathbf{z}. \tag{B.4}$$

We have to make some considerations to prove the well-posedness of each computation, as previously discussed for similar steps. We write explicitly $\tilde{A}^T_{\mathbf{z}\eta}$ in matrix form:

$$\tilde{A}^T_{\mathbf{z}\eta} = \begin{bmatrix} 0 & 0 & A^T_{up} \\ 0 & A^T_{u_s\lambda_{fs}} & A^T_{u\lambda_{fs}} \end{bmatrix} - \begin{bmatrix} A_{p\xi} A^{inv}_{\xi\lambda_e} A_{\lambda_e s} & 0 & 0 \\ 0 & 0 & 0 \end{bmatrix}. \tag{B.5}$$

The matrix product $A_{\eta q_e} A^{-1}_{q_e q_e} A_{q_e \mathbf{z}}$ has one single, non-zero block since the matrix $A_{\lambda_{fs}\xi}$ is null. Indeed, no contribution from the fluid domain displacement appears in the equation for the multiplier λ_{fs}. This equation states the continuity of the velocity between the fluid and the structure on the FSI interface Γ_{fs} and the fluid domain displacement plays no role. The ranks of the matrices $A^T_{\mathbf{z}\eta}$ and $\tilde{A}^T_{\mathbf{z}\eta}$ are the same. For this reason, we can prove that the matrix $\tilde{A}^T_{\mathbf{z}\eta} \tilde{M}^{-1}_{\mathbf{zz}} A_{\mathbf{z}\eta}$, which must be inverted to define the projector Π^T, is indeed invertible once we choose compatible finite elements for $\mathbf{z}$ and $\boldsymbol{\eta}$, i.e. satisfying the inf-sup condition (Babuška, 1973; Brezzi, 1974). Combining (B.1) and (B.4), the projector is defined as:

$$\Pi^T = I - \tilde{M}^{-1}_{\mathbf{zz}} A_{\mathbf{z}\eta} \left[\tilde{A}^T_{\mathbf{z}\eta} \tilde{M}^{-1}_{\mathbf{zz}} A_{\mathbf{z}\eta}\right]^{-1} \tilde{A}^T_{\mathbf{z}\eta}. \tag{B.6}$$

Appendix C. Proof of equivalence of the eigenvalue problems

We start proving that the projected system (30) preserves the spectrum of the system without the fluid domain variables (32). Then, we verify that the system with the fluid domain variables (34) maintains the spectrum. By definition of $\boldsymbol{A} = \Pi^T \tilde{M}^{-1}_{\mathbf{zz}} \tilde{A}_{\mathbf{zz}}$, we write the eigenvalue problem (30) as:

$$\Pi^T \tilde{M}^{-1}_{\mathbf{zz}} \tilde{A}_{\mathbf{zz}} \mathbf{v} = \lambda \mathbf{v}. \tag{C.1}$$

Using the definition of Π^T and pre–multiplying by $\tilde{M}_{\mathbf{zz}}$ we get:

$$\tilde{A}_{\mathbf{zz}} \mathbf{v} + A_{\mathbf{z}\eta} \boldsymbol{\eta}_{\mathbf{v}} = \lambda \tilde{M}_{\mathbf{zz}} \mathbf{v}. \tag{C.2}$$

Moreover, because $\mathbf{v} \in \mathrm{Ker}(\tilde{A}^T_{\mathbf{z}\eta})$, we know that:

$$\tilde{A}^T_{\mathbf{z}\eta} \mathbf{v} = 0. \tag{C.3}$$

Looking at the Eqs. (C.2) and (C.3) and comparing them with the eigenvalue problem (32), we can conclude once we recovered the definition of $\tilde{M}$ and $\tilde{A}$.

Now, we prove that the elimination of the fluid domain variables preserves the spectrum. We can write (33) as:

$$A_{q_e \mathbf{z}} \mathbf{v} + A_{q_e q_e} \boldsymbol{q}_{e\mathbf{v}} = 0, \tag{C.4}$$

that is exactly the third row of the problem (34). Now, we expand the Eq. (C.3) introducing the definition of $\tilde{A}^T_{\mathbf{z}\boldsymbol{\eta}}$ and the definition of the fluid domain variables in (33). We obtain:

$$A^T_{\mathbf{z}\boldsymbol{\eta}} \mathbf{v} + A_{\eta q_e} \boldsymbol{q}_{e\mathbf{v}} = 0, \tag{C.5}$$

that is exactly the second row of the problem (34). Now we can conclude the proof expanding the Eq. (C.2) recovering the definition of the ˜ variables. We get:

$$A_{\mathbf{zz}} \mathbf{v} + A_{\mathbf{z}\boldsymbol{\eta}} \boldsymbol{\eta}_{\mathbf{v}} + A_{\mathbf{z}q_e} \boldsymbol{q}_{e\mathbf{v}} = \lambda (M_{\mathbf{zz}} \mathbf{v} + M_{\mathbf{z}q_e} \boldsymbol{q}_{e\mathbf{v}}), \tag{C.6}$$

that is exactly the first row of the problem (34). Hence, we proved that both the elimination of the fluid domain variables and of the multipliers do not affect the spectrum of the system (34). The multipliers $\boldsymbol{\eta}_{\mathbf{v}}$ and the fluid domain variables $\boldsymbol{q}_{e_{\mathbf{v}}}$ components of the eigenvectors of the full system can be retrieved from $\mathbf{v}$ using the relations (31) and (33). Notice that we have the same property for the adjoint eigenvalue problems and the generalized eigenproblems.

Appendix D. Effect of Reynolds number and Young's modulus

We perform additional tests to illustrate the role of the parameters of the FSI problem in the control of this system. In particular, we investigate the effect of changing the Reynolds number Re, while keeping the initial value of the Young's modulus $E = 20170$, and the effect of changing the Young's modulus, while keeping the initial value of the Reynolds number $Re = 200$. A change of the parameters of the problem affects the spectrum of the uncontrolled scenario and, as consequence, its unstable subspace. In the following, we discuss each new set of parameters describing the corresponding unstable spectrum. We define a feedback matrix by the projection of the system onto the new unstable space and solving a Riccati equation of small dimension for each new case, with the same strategy already discussed. In order to maintain the discussion focused on the role of the problem parameters, and not on the controller design choices, we use the configuration with four couples of actuators placed at the longitudinal positions $x_c = [0.75, 1.3, 2.2, 3.0]$ and select $\omega = 0$. In the sequel, every time marching simulation has been performed by using the same inlet perturbation employed before, defined by a parabolic profile and an amplitude coefficient $\beta = 5\,\%$.

D.1. Effect of the r Reynolds number

In order to evaluate the effect of the Reynolds number, we compare three test cases with $E = 20170$ and $Re = [150, 200, 250]$. The case of $Re = 200$ is the reference case already discussed in Section 4. We expect that a larger Reynolds number leads to a destabilization of the system and a decrease of it results in a stabilization of the modes. For $Re = 150$, the unstable spectrum for the uncontrolled case consists of two pairs of complex conjugate eigenvalues $\lambda_{1,2} = 0.230 \pm 2.34i$ and $\lambda_{3,4} = 0.0163 \pm 1.41i$, that are mirrored with respect to the imaginary axis as soon as we close the loop designing a controller with $\omega = 0$. For $Re = 250$, the unstable spectrum consists of six complex conjugate modes $\lambda_{1,2} = 0.405 \pm 2.33i$, $\lambda_{3,4} = 0.238 \pm 1.67i$ and $\lambda_{5,6} = 0.0724 \pm 0.329i$ that are mirrored with respect to the imaginary axis in the closed loop controlled case. We report in Fig. D.1 the error with respect to the steady state of the time marching simulation subject to the inlet disturbance and we plot the energy of the control inputs required to achieve a stabilization. We observe that the larger the Reynolds number the larger the amplification of the inlet disturbance because the peak of the error that appears around a time $t \approx 20$ increases with Re. However, each controller designed in the linear framework still stabilizes the nonlinear FSI system for each Reynolds number. Looking at the control input energy in Fig. D.1, we note that a much larger effort is required for the highest Reynolds number case and a much smaller one for the lowest Reynolds number, as expected.

D.2. Effect of the Young's modulus

The role of the Young's modulus in the context of the control of this FSI configuration is investigated in the following. A fixed value of the Reynolds number $Re = 200$ is considered and we pick three values for $E = [5 \times 10^3, 2.017 \times 10^4, 1 \times 10^5]$, where the case $E = 2.017 \times 10^4$ is the reference case already discussed in Section 4. A modification of the Young's modulus strongly modifies the uncontrolled spectrum because it results in a modification of the natural frequencies of the splitter plate, leading to possibly different interactions with the fluid. A deep investigation of the role of the Young's modulus on the stability of a similar configuration is performed in Pfister and Marquet (2020). We discuss firstly the case with $E = 5 \times 10^3$. The unstable spectrum consists of three complex conjugate pairs of modes: $\lambda_{1,2} = 0.430 \pm 1.87i$, $\lambda_{3,4} = 0.294 \pm 2.72i$ and $\lambda_{5,6} = 0.0503 \pm 0.259i$ that are mirrored with respect to the imaginary axis in the closed loop case by the controller designed by choosing $\omega = 0$. The case with the stiffer splitter plate, corresponding to $E = 1 \times 10^5$ presents an unstable spectrum with a pair of complex conjugate eigenvalues $\lambda_{1,2} = 0.325 \pm 1.77i$ and a real unstable eigenvalue $\lambda_3 = 0.117$ that are stabilized by the feedback controller. The results of the time marching simulation are reported in Fig. D.2, where we observe that each controller stabilizes the system for all the test cases discussed. Comparing the results of the more flexible case with the reference one, we observe that the error with respect to the steady solution is only slightly increased. However, to stabilize the system, the controller requires a much larger control input energy with respect to the reference

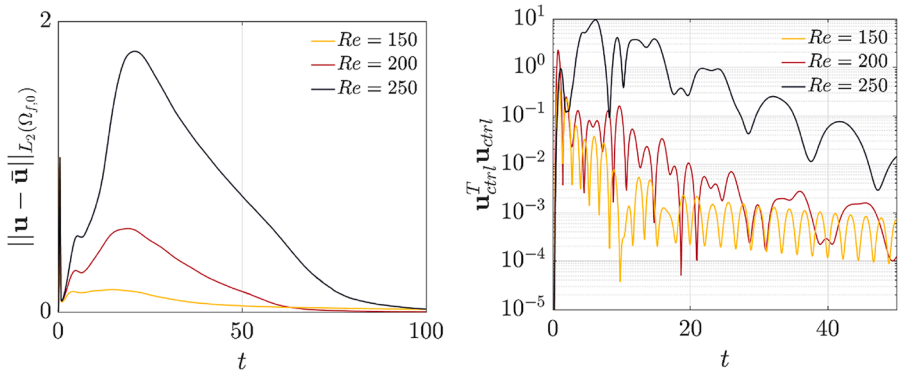

(a) Velocity field error in $L_2(\Omega_{f,0})$ norm. (b) Control input energy $\mathbf{u}_{ctrl}^T \mathbf{u}_{ctrl}$.

Fig. D.1. Effect of the Reynolds number on the control effectiveness in the nonlinear regime, Re = [150, 200, 250].

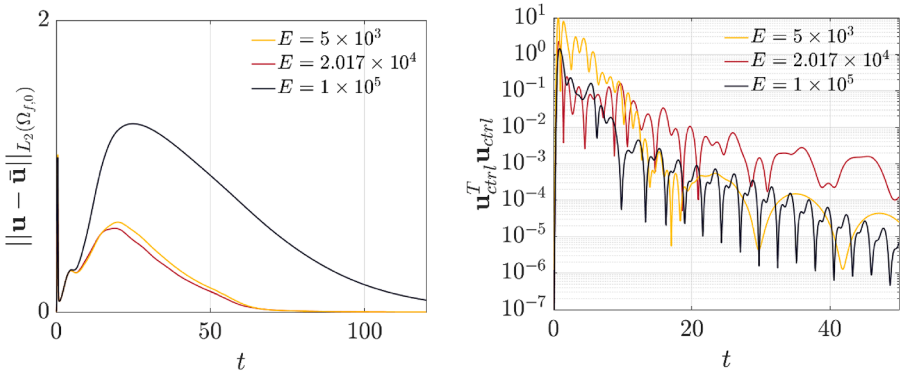

(a) Velocity field error in $L_2(\Omega_{f,0})$ norm. (b) Control input energy $\mathbf{u}_{ctrl}^T \mathbf{u}_{ctrl}$.

Fig. D.2. Effect of the Young's modulus on the control effectiveness in the nonlinear regime, $E = [5 \times 10^3, 2.017 \times 10^4, 1 \times 10^5]$.

cases, especially for the first steps when $t < 15$. In the stiffest configuration, the system exhibits a markedly different behaviour compared to the reference scenario. The inlet amplitude is significantly amplified for these FSI parameters, leading to a slower stabilization process. Nevertheless, it is worth noting that the control input energy required to stabilize the system is the lowest among the three configurations considered. This outcome can be attributed to the reduced compliance of this configuration, which makes it less susceptible to structural oscillations.

References

Abdelkefi, A., 2015. Aeroelastic energy harvesting: a review.

Airiau, C., Buchot, J.M., Dubey, R.K., Fournié, M., Raymond, J.P., Weller-Calvo, J., 2017. Stabilization and best actuator location for the navier-stokes equations.

Auteri, F., Bettini, P., Bonfanti, N., 2021. Scaling Laws for an Airfoil with MFC-Actuated Trailing Edge Plate. Vol. 147 of *Cham*. Springer.

Babuška, I., 1973. The finite element method with lagrangian multipliers.

Bagheri, S., kervik, E.A., Brandt, L., Henningson, D.S., 2009. Matrix-free methods for the stability and control of boundary layers aiaa.

Bilgen, O., Butt, L., Day, S., Sossi, C., Weaver, J., Wolek, A., Mason, W., Inman, D., 2011. A novel unmanned aircraft with solid-state control surfaces: analysis and flight demonstration. In: Structural Dynamics and Materials Conference.

Bilgen, O., Friswell, M.I., 2014. Piezoceramic composite actuators for a solid-state variable-camber wing.

Boffi, D., 2010. Finite element approximation of eigenvalue problems. Acta Numer. 19, 1–120.

Brezzi, F., 1974. On the existence, uniqueness and approximation of saddle-point problems arising from lagrangian multipliers.

Carini, M., Pfister, J.L., Marquet, O., 2017. Fluid-solid-electric stability analysis and passive control of a piezoelectric flexible plate clamped on a rigid cylinder. AIMETA XXIII Conference.

Chen, C.T., 1995. Linear System Theory and Design. Inc., USA, Oxford University Press. 2nd. ed.

Côté, F., Masson, P., Mrad, N., Cotoni, V., 2004. Dynamic and static modelling of piezoelectric composite structures using a thermal analogy with msc/nastran.

Fournié, M., Ndiaye, M., Raymond, J.P., 2019. Feedback stabilization of a two-dimensional fluid-structure interaction system with mixed boundary conditions.

Hecht, F., 2012. New development in freefem.

IEEE Standard on Piezoelectricity In: ANSI/IEEE Std 176-1987, pp. 0_1-, 1988.

Kesavan, S., Raymond, J.P., 2009. On a Degenerate Riccati Equation.

Lehoucq, R.B., Sorensen, D.C., Yang, C., 1998. Philadelphia.

Loiseau, J.C., Bucci, M.A., Cherubini, S., Robinet, J.C., 2019. Time-stepping and krylov methods for large-scale instability problems. computational modelling of bifurcations and instabilities in fluid dynamics.

Monner, H., Riemenschneider, J., Opitz, S., Schulz, M., 2011. Development of Active Twist Rotors at the German Aerospace Center (DLR). AIAA, 2011-1824. 52nd AIAA/ASME/ASCE/AHS/ASC Structures, Structural Dynamics and Materials Conference.
Moreno, J.C., Mora, R.B., Sevillano, A.A.R., González, A.C., 2023. Performance enhancement of a bioinspired micro air vehicle by integrating a smart composite in its morphing wing.
'NASA Invention of the Year' Controls Noise and Vibration , 2007. https://ntrs.nasa.gov/citations/20080003909.
Pedraglio, S., 2015. Linear Stability Analysis in FSI Problems Including Large Displacements. Technical Report. M. S. thesis.
Pfister, J.L., Marquet, O., 2020. Fluid-structure stability analyses and nonlinear dynamics of flexible splitter plates interacting with a circular cylinder flow.
Pfister, J.L., Marquet, O., Carini, M., 2019. Linear stability analysis of strongly coupled fluid-structure problems with the arbitrary-lagrangian-eulerian method.
Raymond, J.P., 2006. Feedback boundary stabilization of the two-dimensional navier-stokes equations.
Renard, Y., Poulios, K., 2020. GetFEM: automated fe modeling of multiphysics problems based on a generic weak form language.
Russo, N., Gonzalez, L.M., Viccione, G., Pisacreta, C., 2020. A control mechanism of a typical fluid-structure interaction problem based on dielectric barrier discharge plasma actuation model.
Smart Material website https://www.smart-material.com/MFC-product-mainV2.html.
Shamanskiy, A., Simeon, B., 2021. Mesh moving techniques in fluid-structure interaction: robustness, accumulated distortion and computational efficiency. Comput. Mech. 67, 583–600.
Soti, A.K., Thompson, M.C., Sheridan, J., Bhardwaj, R., 2017. Harnessing electrical power from vortex-induced vibration of a circular cylinder.
Sun, J., Guan, Q., Liu, Y., Leng, J., 2016. Morphing aircraft based on smart materials and structures: a state-of-the-art review.
Thomas, O., Deü, J.F., Ducarne, J., 2009. Vibrations of an elastic structure with shunted piezoelectric patches: efficient finite element formulation and electromechanical coupling coefficients.
Turek, S., Hron, J., 2006. Proposal for Numerical Benchmarking of Fluid-Structure Interaction between an Elastic Object and Laminar Incompressible Flow. Vol. 53. Springer, Berlin, Heidelberg.